Polymer 347 (2026) 129674

Contents lists available at ScienceDirect

Polymer

journal homepage: www.elsevier.com/locate/polymer

Multistep synthesis of heterocyclic Schiff base–derived polybenzoxazines for direct carbonization into N, O, S–co-doped microporous carbons with dual CO_2 capture and supercapacitor performance

Yun-Chien Zheng [a], Shimaa Abdelnaser [a,b], Yousra M. Nabil [a,b], Mostafa Sayed [c], Shiao-Wei Kuo [a], Chih-Feng Wang [a,d,*], Mostafa Ahmed [c,**], Ahmed F.M. EL-Mahdy [a,b,***]

[a] Department of Materials and Optoelectronic Science, National Sun Yat-Sen University, Kaohsiung, 80424, Taiwan
[b] Chemistry Department, Faculty of Science, Assiut University, Assiut, 71516, Egypt
[c] Chemistry Department, Faculty of Science, New Valley University, El-Kharja, 72511, Egypt
[d] Institute of Advanced Semiconductor Packaging and Testing, National Sun Yat-Sen University, Kaohsiung, 80424, Taiwan

ARTICLE INFO

Keywords:
Polybenzoxazine-derived porous carbons
Supercapacitors
CO_2 capture

ABSTRACT

The rising demand for sustainable energy storage and carbon mitigation calls for multifunctional materials that integrate high surface area, tailored heteroatom chemistry, and robust electrochemical stability. Herein, we report a continuous three-step synthesis of two novel heterocyclic Schiff base–derived benzoxazine monomers—3-(6-methoxybenzo [d]thiazol-2-yl)-3,4-dihydro-2H-benzo[e][1,3]oxazine (SA-tz Bz) and 3-(6-methoxybenzo [d]thiazol-2-yl)-3,4-dihydro-2H-naphtho[2,1-e][1,3]oxazine (NA-tz Bz)—through sequential Schiff base formation, reduction, and Mannich condensation. Thermal ring-opening polymerization followed by direct carbonization at 600 and 700 °C under an inert atmosphere yielded N, O, S co-doped microporous carbons (C@poly (SA-tz Bz) and C@poly (NA-tz Bz)) without the need for activating agents or wastewater generation. These heteroatom-enriched carbons exhibit disordered amorphous structures with hierarchical porosity, abundant pyridinic/pyrrolic nitrogen species, and oxygen/sulfur functionalities, as confirmed by BET, Raman, XPS, and TEM analyses. Electrochemical studies revealed that C@poly (NA-tz Bz 700) delivers a high specific capacitance of 423 ± 18 F g^{-1} at 0.5 A g^{-1} in a three-electrode system, good cycling stability (98 % retention after 6000 cycles), and superior performance in a symmetric two-electrode device (342 F g^{-1}, 89.50 % retention after 4000 cycles). Moreover, C@poly (NA-tz Bz 700) achieves an exceptional CO_2 adsorption capacity of 231.7 cm^3 g^{-1} at 273 K, surpassing many reported heteroatom-doped carbons. This work presents a sustainable strategy for designing heterocyclic benzoxazine-derived microporous carbons that combine efficient energy storage with effective CO_2 capture, offering promising prospects for next-generation electrochemical and environmental applications.

1. Introduction

The alarming rise in atmospheric carbon dioxide (CO_2) concentrations, mainly stemming from the extensive use of fossil fuels, is one of the most critical contributors to global warming and climate change [1–3]. As international efforts focus on limiting carbon emissions, carbon capture and storage (CCS) technologies have emerged as a viable route for mitigating anthropogenic CO_2 emissions [4]. Among the various capture methods developed—such as chemical absorption using amines, membrane separation, and adsorption—solid sorbents have received increasing attention due to their operational simplicity, cost-effectiveness, and relatively low energy requirements for regeneration [5–9]. Porous carbon-based materials are particularly attractive for CO_2 adsorption because of their high surface area, tunable porosity, robust chemical and thermal stability, and ease of functionalization [10]. However, the intrinsic physisorption characteristics of unmodified carbon materials often result in limited CO_2 uptake under ambient conditions [11]. To overcome this limitation, the incorporation of

* Corresponding author. Department of Materials and Optoelectronic Science, National Sun Yat-Sen University, Kaohsiung, 80424, Taiwan.
** Corresponding author.
*** Corresponding author. Department of Materials and Optoelectronic Science, National Sun Yat-Sen University, Kaohsiung, 80424, Taiwan.
E-mail addresses: cfwang@mail.nsysu.edu.tw (C.-F. Wang), drmostafa@scinv.au.edu.eg (M. Ahmed), ahmedelmahdy@mail.nsysu.edu.tw (A.F.M. EL-Mahdy).

https://doi.org/10.1016/j.polymer.2026.129674
Received 24 October 2025; Received in revised form 14 January 2026; Accepted 28 January 2026
Available online 29 January 2026

heteroatoms—especially nitrogen (N), oxygen (O), and sulfur (S)—into the carbon framework has been widely explored [4]· [12–17]. Heteroatom doping introduces polar sites and modifies the electronic environment of the carbon matrix, thereby enhancing interactions with the quadrupolar CO_2 molecules through hydrogen bonding, dipole-quadrupole interactions, and acid-base chemistry. Nitrogen-doped carbons, in particular, exhibit increased CO_2 affinity due to the presence of pyridinic and pyrrolic sites, while sulfur doping further enhances surface roughness and selectivity toward CO_2 over nitrogen [18]. Co-doping with N and S often leads to synergistic effects, where the combined functionalities facilitate higher adsorption capacities, greater selectivity, and improved thermal and chemical robustness [19]. These attributes render heteroatom-doped carbons exceptionally promising candidates for next-generation CO_2 capture technologies that focus on reducing greenhouse gas emissions and facilitating carbon recycling processes [20,21].

In parallel with environmental concerns, the global transition toward sustainable energy systems demands the development of efficient and durable energy storage devices [22–28]. Supercapacitors have emerged as a leading technology due to their rapid charge–discharge capability, long cycle life, and high-power density [29–33]. The performance of supercapacitors is mainly determined by the properties of the electrode materials. Porous carbon materials are widely utilized in this context due to their high conductivity and large surface area, facilitating electric double-layer formation and rapid ion transport. However, to further improve their energy storage capability, heteroatom doping has been extensively adopted. Nitrogen atoms introduce redox-active sites and improve surface wettability, thereby contributing to pseudocapacitance and enhancing the charge storage mechanism. Sulfur and oxygen doping also play significant roles by altering the surface chemistry and electronic distribution, which results in better electrochemical performance, especially at high current densities. Co-doping strategies that integrate multiple heteroatoms create a synergistic framework that not only increases ion accessibility but also enhances charge transfer kinetics. As a result, heteroatom-doped porous carbons are at the forefront of research in energy storage technologies, especially for high-performance supercapacitors [34–36].

The preparation of heteroatom-doped carbon materials can be achieved through several synthesis routes, including chemical activation, templated synthesis, hydrothermal treatment, and direct carbonization. Among these, direct carbonization stands out as an environmentally friendly and scalable approach. This method involves thermal treatment of organic precursors inherently rich in heteroatoms, typically under an inert atmosphere at elevated temperatures (e.g., 700 °C). Unlike chemical activation with reagents like KOH, which may result in corrosive byproducts and wastewater, direct carbonization eliminates the need for external activating agents. It simplifies the process and minimizes environmental hazards. Moreover, this technique allows precise control over pore structure and dopant distribution by carefully selecting and designing the precursor molecules. As such, direct carbonization is regarded as an efficient and green strategy for producing functionalized carbon materials tailored for both gas adsorption and electrochemical applications [25,37–39]. Among the variety of precursors explored for synthesizing heteroatom-doped porous carbons, polybenzoxazines (PBZs) have gained considerable interest due to their unique structural and functional attributes. PBZs are a class of thermosetting resins synthesized via the Mannich condensation of phenols, primary amines, and formaldehyde [30–42]. These polymers are characterized by their oxazine rings containing nitrogen and oxygen, which are retained during pyrolysis and contribute to the final carbon's dopant content [43]. PBZs exhibit exceptional thermal stability, low water absorption, high char yield, flame retardance, and low dielectric constants, making them highly suitable for conversion into porous carbon materials [43,44]. The ring-opening polymerization of PBZs occurs without the need for external catalysts, resulting in highly cross-linked networks that are dimensionally stable and structurally robust [43]. Furthermore, the molecular structure of PBZs can be readily tailored by selecting appropriate monomers, enabling the inclusion of additional heteroatoms such as sulfur through functional group substitution. Upon carbonization, PBZ-derived carbons exhibit hierarchical porosity and a high degree of heteroatom doping, resulting in materials with exceptional performance in both CO_2 capture and supercapacitor applications [45]. In this context, the synthesis of N, O, and S co-doped carbon materials through the direct carbonization of tailored polybenzoxazines represents a promising route toward multifunctional materials for addressing urgent environmental and energy-related challenges. The integration of sustainable synthesis methods, adjustable heteroatom chemistry, and advanced functional properties positions these materials as strong candidates for practical implementation in carbon capture systems and energy storage technologies.

Based on this rationale, we successfully synthesized two novel heterocyclic Schiff base–derived benzoxazine monomers, 3-(6-methoxybenzo[d]thiazol-2-yl)-3,4-dihydro-2H-benzo[e][1,3]oxazine (SA-tz Bz) and 3-(6-methoxybenzo[d]thiazol-2-yl)-3,4-dihydro-2H-naphtho[2,1-e][1,3]oxazine (NA-tz Bz), via a continuous three-step procedure involving Schiff base formation, reduction, and Mannich condensation, starting from the Schiff base precursor 6-methoxybenzo[d]thiazol-2-amine (TZ-NH_2) (Scheme 1a). Specifically, the condensation of TZ-NH_2 with salicylaldehyde (SA-OHCHO) and 1-hydroxy-2-naphthaldehyde (NA-OHCHO) afforded the intermediates TZ-hydroxybenzylimine (2-(((6-methoxybenzo[d]thiazol-2-yl)imino)methyl)phenol) and TZ-hydroxynaphthylmethylimine (2-(((5-methoxybenzo[d]thiazol-2-yl)imino)methyl)naphthalen-1-ol), which were subsequently reduced using $NaBH_4$ to yield TZ-hydroxybenzylamine (2-(((6-methoxybenzo[d]thiazol-2-yl)amino)methyl)phenol) and TZ-hydroxynaphthylmethylamine (2-(((6-methoxybenzo[d]thiazol-2-yl)amino)methyl)naphthalen-1-ol). These intermediates underwent Mannich condensation with formaldehyde to afford the target benzoxazine monomers SA-tz Bz and NA-tz Bz (Scheme 1a). These monomers were then subjected to thermal ring-opening polymerization to form poly (SA-tz Bz) and poly (NA-tz Bz) (Scheme 1b). Subsequent direct carbonization of the resulting polymers at two temperatures (600 and 700 °C) under nitrogen produced N, O, and S co-doped microporous carbons, referred to as C@poly (SA-tz Bz 600), C@poly (SA-tz Bz 700), C@poly (NA-tz Bz 600) and C@poly (NA-tz Bz 700) (Scheme 1b). The chemical structures and thermal curing behaviors of SA-tz Bz and NA-tz Bz were verified using ^1H and ^{13}C NMR spectroscopy, FTIR, DSC, and TGA analyses. In addition, porosity and morphology analyses of the resulting carbon materials reveal predominantly amorphous structures along with enhanced specific surface areas. Among these heteroatom-doped carbons, we will focus on the C@poly (SA-tz Bz 700) and C@poly (NA-tz Bz 700) materials in this research, as they exhibit high specific capacitance and good CO_2 capture performance, highlighting their potential for integration into advanced energy storage systems, gas separation technologies, and environmental remediation platforms [46].

2. Experimental section

2.1. Materials

Ethanol (EtOH, ≥99.5 %), sodium borohydride ($NaBH_4$), and methanol (MeOH, ≥98 %) were purchased from Sigma-Aldrich. 2-Hydroxybenzaldehyde (SA), 1-hydroxy-2-naphthaldehyde (NA), 6-methoxybenzo[d]thiazol-2-amine (TZ-NH_2), trifluoroacetic acid, formaldehyde (37 %), and piperidine were obtained from Tokyo Chemical Industry.

2.2. Synthesis of 3-(6-methoxybenzo[d]thiazol-2-yl)-3,4-dihydro-2H-benzo[e][1,3]oxazine (SA-tz Bz)

A mixture of TZ-hydroxybenzylamine (1 g, 3.5 mmol) and formaldehyde (37 % in H_2O, 2 mL) in methanol solvent (50 mL) was vigorously

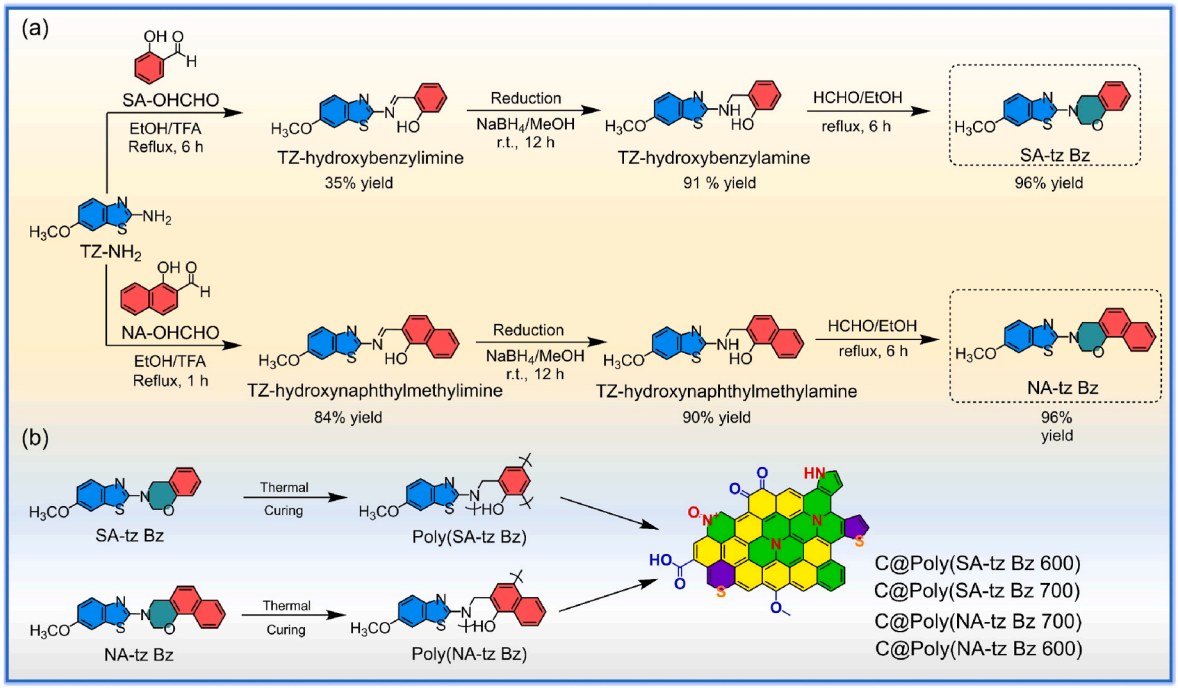

Scheme 1. (a) Schematic illustration of the three-step synthesis of heterocyclic Schiff base–derived benzoxazines (SA-tz Bz, NA-tz Bz). (b) Thermal ring-opening polymerization of SA-tz Bz and NA-tz Bz into poly (SA-tz Bz) and poly (NA-tz Bz), followed by direct carbonization to yield N, O, S co-doped microporous carbons (C@poly (SA-tz Bz 600), (C@poly (SA-tz Bz 700), C@poly (NA-tz Bz 600), and C@poly (NA-tz Bz 700)).

stirred and refluxed at 80 °C temperature under a nitrogen atmosphere for 6 h. Upon complete consumption of the starting material (as monitored by TLC), the resulting precipitate was collected by filtration and washed several times with methanol to remove residual formaldehyde. SA-tz Bz was obtained as a white solid in 96 % yield (1 g) (Scheme 1a). Further experimental details are provided in the ESI.

2.3. Synthesis of 3-(6-methoxybenzo[d]thiazol-2-yl)-3,4-dihydro-2H-naphtho [2,1-e][1,3] oxazine (NA-tz Bz)

TZ-hydroxynaphthylmethylamine (1 g, 3 mmol) and formaldehyde (37 % in H_2O, 2 mL) were dissolved in ethanol solvent (50 mL) and vigorously stirred and refluxed at 80 °C temperature under nitrogen atmosphere for 6 h. After complete conversion of the starting material, which was confirmed by TLC, the resulting precipitate was collected by filtration and washed several times with ethanol to remove the residual formaldehyde, affording NA-tz Bz as a white solid in 96 % yield (0.6 g) (Scheme 1a). Further experimental details are provided in the ESI.

2.4. Synthesis of poly (SA-tz Bz) and poly (NA-tz Bz) polymers

Poly (SA-tz Bz) and poly (NA-tz Bz) polymers were synthesized via ring-opening polymerization of the corresponding SA-tz Bz and NA-tz Bz monomers by heating at 150, 180, 210, 240, and 270 °C for 2 h at each temperature (Scheme 1b). This stepwise program was selected to regulate the exothermic ring-opening polymerization of benzoxazine units and prevent rapid gelation/heat accumulation, thereby ensuring the formation of a homogeneous cross-linked network. The high curing conversion was confirmed by the disappearance of oxazine-associated FTIR bands and the near vanishing of the curing exotherm/enthalpy in DSC at the final stages (240–270 °C; Fig. 3).

2.5. Direct synthesis of N, O, and S co-doped microporous carbons

SA-tz Bz and NA-tz Bz were thermally cured at 240 °C for 24 h to afford poly (SA-tz Bz) and poly (NA-tz Bz), respectively. The obtained polymers were then carbonized in a tubular furnace under a nitrogen atmosphere by heating at a controlled rate of 5 °C min^{-1} to the target temperature (600 or 700 °C), holding for 6 h, and subsequently allowing the furnace to cool naturally to room temperature under N_2. This procedure produced the N-, O-, and S-co-doped porous carbons, denoted as C@poly (SA-tz Bz 600), C@poly (SA-tz Bz 700), C@poly (NA-tz Bz 600), and C@poly (NA-tz Bz 700) (Scheme 1b). The carbon yields were approximately 68 % for C@poly (SA-tz Bz 600), 76 % for C@poly (NA-tz Bz 600), 66 % for C@poly (SA-tz Bz 700), and 72 % for C@poly (NA-tz Bz 700).

3. Results and Discussion

3.1. Synthesis and characteristics of SA-tz Bz and NA-tz Bz monomers

Scheme 1a illustrates a controlled multistep synthetic route toward the heterocyclic Schiff base–derived benzoxazine monomers SA-tz Bz and NA-tz Bz starting from 6-methoxybenzo [*d*]thiazol-2-amine (TZ-NH_2). In the first step, TZ-NH_2 was condensed with either salicylaldehyde (SA-OHCHO) or 1-hydroxy-2-naphthaldehyde (NA-OHCHO) in ethanol under reflux at 80 °C using a catalytic amount of trifluoroacetic acid. Under this acidic reflux condition, nucleophilic attack of the amine nitrogen on the aldehydic carbonyl carbon followed by dehydration led to formation of the corresponding imine (C═N) intermediates, TZ-hydroxybenzylimine and TZ-hydroxynaphthylmethylimine. The significantly different isolated yields (35 % for the salicylaldehyde-derived imine and 84 % for the naphthaldehyde-derived analogue) can be rationalized by the higher π-conjugation and greater stabilization of the imine linkage in the naphthyl system, as well as possible intramolecular hydrogen bonding and partial reversibility of imine formation in the salicylaldehyde case under reflux in ethanol. In the second step, both imine intermediates were reduced using sodium borohydride ($NaBH_4$) in methanol at ambient temperature (approximately 30 °C) for 12 h. These mild conditions enabled selective reduction of the C═N bond without affecting the benzo[*d*]thiazole heterocycle. The high isolated yields obtained for TZ-hydroxybenzylamine (91 %) and TZ-

hydroxynaphthylmethylamine (90 %) indicate efficient hydride transfer and good chemoselectivity of $NaBH_4$ in methanol. Conversion of the rigid imine linkage into a flexible NH–CH_2 unit at this stage is particularly important, as it facilitates subsequent intramolecular cyclization during benzoxazine formation. The final step involved a Mannich condensation between the reduced amine intermediates and formaldehyde (HCHO), carried out under reflux at 80 °C for 6 h with vigorous stirring. Methanol was used as the solvent for SA-tz Bz, whereas ethanol was employed for NA-tz Bz, reflecting solubility considerations of the respective precursors. The benzoxazine ring is formed via a Mannich condensation in which the amine first undergoes *N*-methylolation with formaldehyde, followed by dehydration to an iminium intermediate that is intramolecularly attacked by the ortho-phenolic oxygen, leading to six-membered oxazine ring closure and formation of the stable –O–CH_2–N–CH_2– benzoxazine framework. The high yields obtained for both benzoxazine monomers (96 % for both SA-tz Bz and NA-tz Bz) highlight the efficiency of the intramolecular Mannich cyclization under reflux conditions and the high reactivity of ortho-hydroxylated aromatic systems. The resulting benzoxazine monomers integrate benzo[d]thiazole heterocycles with aromatic units, providing structurally rigid yet functionally versatile platforms for subsequent polymerization and materials-oriented investigations. The FTIR spectra in Fig. 1a–c verifies the stepwise synthesis of SA-tz Bz. The intermediate TZ-hydroxybenzylimine (Fig. 1c) exhibits a characteristic C═N stretching band at 1603 cm^{-1}, while its reduced form, TZ-hydroxybenzylamine (Fig. 1b), shows a broad N–H stretching band at 3359 cm^{-1}, confirming successful reduction of the imine to an amine. The final SA-tz Bz spectrum (Fig. 1a) displays distinct absorption bands at 1218, 1055, and 932 cm^{-1}, corresponding to asymmetric C–O–C stretching, C–O antisymmetric stretching, and oxazine ring vibrations, respectively. Similarly, Fig. 1d–f presents the FTIR spectra for the synthesis of NA-tz Bz. TZ-hydroxynaphthylmethylimine (Fig. 1f) shows a C═N stretching band at 1600 cm^{-1}, while the reduced TZ-hydroxynaphthylmethylamine (Fig. 1e) exhibits an N–H stretching band at 3430 cm^{-1}. The appearance of characteristic bands at 1225, 1051, and 926 cm^{-1} in the final NA-tz Bz spectrum (Fig. 1d) confirms the successful formation of the oxazine ring.

Fig. 2(a–l) illustrates the ^1H and ^{13}C NMR spectra confirming the successful stepwise synthesis of SA-tz Bz and NA-tz Bz from their corresponding Schiff base intermediates. For the SA-tz Bz synthetic pathway (Fig. 2a–c), the ^1H NMR spectrum of TZ-hydroxybenzylimine shows diagnostic signals at 11.58 ppm (phenolic –OH), 9.35 ppm (HC═N proton), 6.82–7.92 ppm (aromatic protons), and 3.84 ppm (O–CH_3), confirming the formation of the Schiff base. After reduction, these imine resonances disappear, and a new NH–CH_2 signal emerges at 4.44 ppm, indicating conversion to TZ-hydroxybenzylamine. The ^1H NMR spectrum of the final SA-tz Bz displays two distinct new signals at 4.94 ppm (OCH_2–N) and 4.74 ppm ($ArCH_2$–N) in a 1:1 ratio, characteristic of Mannich-type cyclization forming the oxazine ring. Corresponding ^{13}C NMR spectra (Fig. 2d–f) show the Schiff base signals at 160.87 ppm (C═N), 161.21 ppm (C–OH), and 136.88–105.57 ppm (aromatic carbons). In the reduced intermediate, new peaks appear at 155.59 ppm (C–OH) and 43.10 ppm (NH–CH_2), whereas the final SA-tz Bz spectrum exhibits signature oxazine carbon peaks at 82.84 ppm (O–CH_2–N) and 55.76 ppm (Ar–CH_2–N), confirming successful ring closure and the absence of the NH–CH_2 signal from the precursor. For the NA-tz Bz synthetic pathway (Fig. 2g–i), the ^1H NMR spectrum of TZ-hydroxynaphthylmethylimine displays peaks at 9.95 ppm (HC═N), 8.80 ppm (phenolic –OH), 7.12–8.13 ppm (aromatics), and 3.86 ppm (O–CH_3), consistent with Schiff base formation. After $NaBH_4$ reduction, the disappearance of the C═N proton and the appearance of a new NH–CH_2 resonance at 4.89 ppm confirm the formation of TZ-hydroxynaphthylmethylamine. The final NA-tz Bz spectrum shows two new resonances at 5.26 ppm (OCH_2–N) and 4.63 ppm ($ArCH_2$–N) in an approximate 1:1 ratio, confirming successful Mannich condensation. In the ^{13}C NMR spectra (Fig. 2j–l), the imine intermediate shows signals at 160.58 ppm (C═N), 163.42 ppm (C–OH), and 142.38–105.00 ppm (aromatic carbons). After reduction, peaks at 153.21 ppm (C–OH) and 37.95 ppm (NH–CH_2) appear, while the final NA-tz Bz spectrum exhibits distinct oxazine carbon signals at 80.76 ppm (O–CH_2–N) and 55.62 ppm (Ar–CH_2–N) with the disappearance of NH–CH_2, confirming complete ring closure and the high purity of the heterocyclic benzoxazine product.

3.2. Thermal ring-opening polymerization of the SA-tb Bz and NA-tz Bz

The thermal curing behaviors of both SA-tz Bz and NA-tz Bz monomers were investigated using temperature-dependent FTIR spectroscopy, differential scanning calorimetry (DSC), and thermogravimetric analysis (TGA) at different heating stages (Fig. 3). The FTIR spectra of SA-tz Bz recorded at temperatures from 150 to 270 °C (Fig. 3a) were used to monitor its thermal polymerization behavior. The characteristic absorption bands of the C–O–C and oxazine ring at 1218, 1055, and 932 cm^{-1} progressively decreased with increasing temperature and disappeared at 240 °C, indicating the occurrence of ring-opening polymerization. The DSC thermogram of uncured SA-tz Bz (Fig. 3b) shows a distinct and sharp exothermic curing peak at 308 °C with a reaction enthalpy of 100.2 J g^{-1}, indicating the initiation of the thermal ring-opening polymerization of the oxazine monomer and confirming its high purity. After partial thermal treatments at 150, 180, and 210 °C, the exothermic peaks gradually shifted to 306, 301, and 283 °C, respectively, accompanied by changes in reaction enthalpy to 134.5, 106.5, and 7.8 J g^{-1}. This progressive shift to lower temperatures and reduction

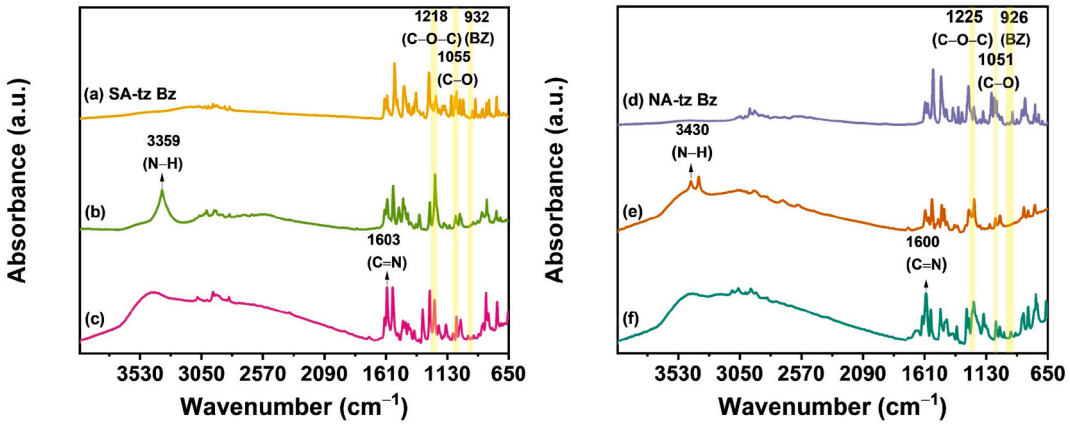

Fig. 1. The FTIR spectra of (a) SA-tz Bz, (b) TZ-hydroxybenzylimine, (c) TZ-hydroxybenzylamine, (d) NA-tz Bz, (e) TZ-hydroxynaphthylmethylamine, and (f) TZ-hydroxynaphthylmethylimine.

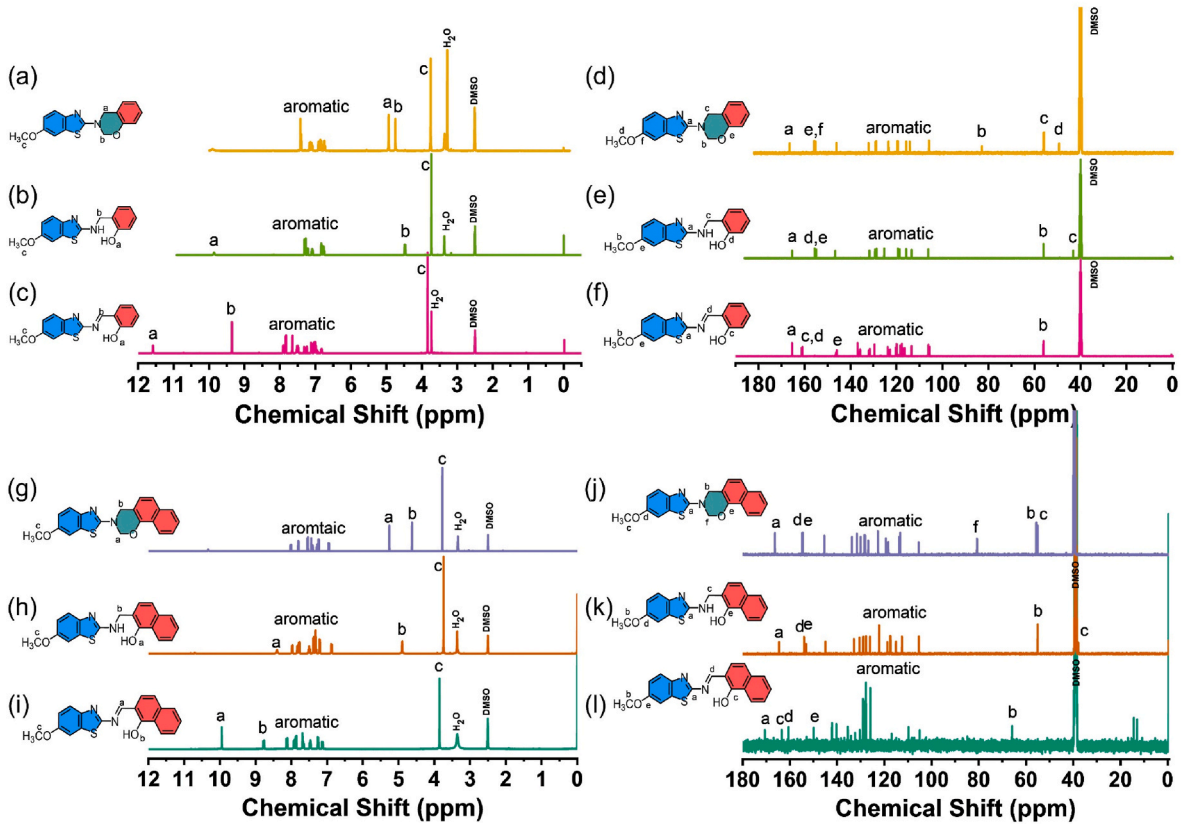

Fig. 2. (a) ^{1}H NMR spectra of (a) SA-tz Bz, (b) TZ-hydroxybenzylimine, (c) TZ-hydroxybenzylamine, (d) NA-tz Bz, (e) TZ-hydroxynaphthylmethylamine, and (f) TZ-hydroxynaphthylmethylimine. ^{13}C NMR spectra of (g) SA-tz Bz, (h) TZ-hydroxybenzylimine, (i) TZ-hydroxybenzylamine, (j) NA-tz Bz, (k) TZ-hydroxynaphthylmethylamine, and (l) TZ-hydroxynaphthylmethylimine.

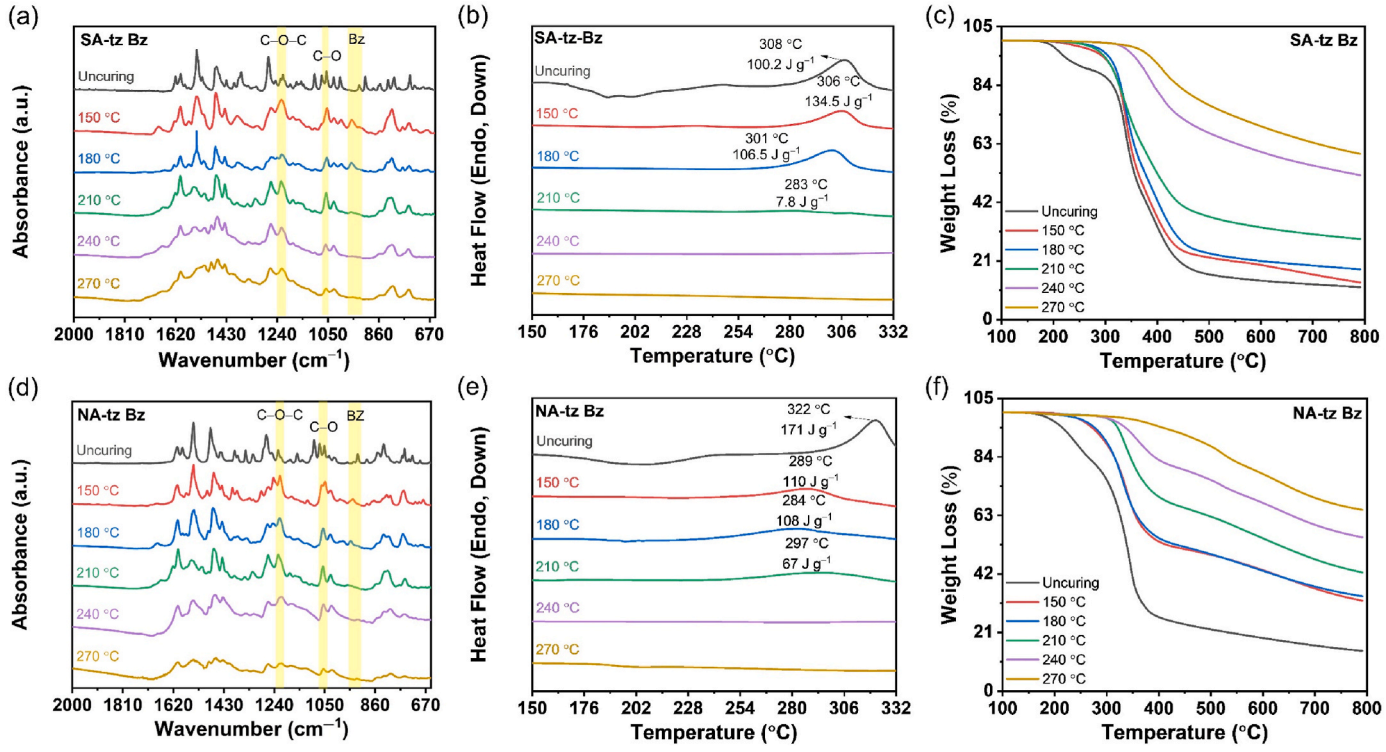

Fig. 3. FTIR (a,d), DSC (b,e), and TGA (c,f) analyses of (a–c) SA-tz Bz and (d–f) NA-tz Bz in the uncured state and following thermal treatment at temperatures ranging from 150 to 270 °C.

in heat release reflects the stepwise advancement of the curing reaction. As the pre-curing temperature increased, the intensity of both endothermic and exothermic events weakened markedly, and the curing peak almost disappeared after treatment at 240 °C, signifying that most oxazine rings had undergone complete ring-opening polymerization to form a highly cross-linked poly (SA-tz Bz) network. By 270 °C, no noticeable exothermic transition remained, confirming the completion of the curing process. These DSC results align well with the FTIR data (Fig. 3a), which showed the gradual disappearance of the characteristic oxazine ring vibrations during thermal curing. Moreover, TGA analysis (Fig. 3c) shows that the uncured SA-tz Bz begins to degrade at relatively low temperatures, with a temperature at which a 5 % weight loss (T_{d5}) = 216 °C and a temperature at which a 10 % weight loss (T_{d10}) = 263 °C, reflecting the onset of oxazine ring opening and the release of volatile by-products. After thermal pre-curing at 150 °C, the T_{d5} and T_{d10} values shift to 292 °C and 314 °C, respectively, while curing at 180 °C further increases them to 293 °C and 312 °C, indicating partial advancement of the polymerization process. A more pronounced improvement is observed for the 210 °C-treated sample, which shows T_{d5} = 302 °C and T_{d10} = 319 °C, along with a higher char yield, confirming the formation of a partially cross-linked poly (SA-tz Bz) network. Upon curing at 240 °C and 270 °C, the materials display the highest thermal resistance, reaching T_{d5} = 352 °C/T_{d10} = 373 °C and T_{d5} = 381 °C/T_{d10} = 408 °C, respectively, with markedly reduced weight-loss rates and maximum char residues (as summarized in Table S1). These results demonstrate that higher pre-curing temperatures promote more extensive ring-opening polymerization and cross-linking, which reduce chain mobility and enhance the thermal robustness of the resulting polymer network. This progressive improvement in thermal stability with curing temperature is consistent with the FTIR and DSC results, confirming the complete conversion of SA-tz Bz monomers into thermally stable poly (SA-tz Bz). These findings indicate that temperatures above 210 °C are required to effectively initiate and complete the ring-opening polymerization of the SA-tz Bz monomer.

The FTIR spectra of NA-tz Bz recorded at temperatures from 150 to 270 °C (Fig. 3d) were used to track its thermal polymerization behavior. The characteristic C–O–C and oxazine ring bands at 1225, 1051, and 926 cm^{-1} gradually decreased in intensity with increasing temperature and completely disappeared at 240 °C, confirming the progressive ring-opening polymerization of the oxazine units. The DSC thermogram of uncured NA-tz Bz (Fig. 3e) shows a sharp exothermic curing peak at 322 °C with a reaction enthalpy of 171 J g^{-1}, indicating the initiation of the thermal polymerization and confirming the high purity of the monomer. After partial pre-curing at 150, 180, and 210 °C, the exothermic peaks shifted to 289, 284, and 297 °C, respectively, accompanied by decreased reaction enthalpies of 110, 108, and 67 J g^{-1}, demonstrating the gradual advancement of the curing reaction. As the pre-curing temperature increased, the intensity of the thermal events diminished, and the curing peak disappeared almost entirely after treatment at 240 °C, signifying extensive ring-opening and the formation of a cross-linked poly (NA-tz Bz) network. At 270 °C, no exothermic transition remained, confirming complete curing. Consistent with these observations, TGA analysis (Fig. 3f) shows that uncured NA-tz Bz begins to degrade at relatively low temperatures, with T_{d5} = 211 °C and T_{d10} = 237 °C, reflecting the onset of thermal decomposition and volatile release. After pre-curing at 150 °C, the T_{d5} and T_{d10} values increased to 268 and 294 °C and further increased to 274 and 298 °C after curing at 180 °C, indicating enhanced thermal stability from partial polymerization. A more significant improvement was observed for the 210 °C-treated sample T_{d5} = 319 °C; T_{d10} = 332 °C), accompanied by a higher char yield, confirming the development of a partially cross-linked polymer network. After curing at 240 and 270 °C, NA-tz Bz exhibited the highest thermal resistance, with T_{d5} = 332 °C/T_{d10} = 359 °C and T_{d5} = 398 °C/T_{d10} = 475 °C, respectively, along with reduced weight-loss rates and maximum char residues (Table S2). These findings show that increasing the pre-curing temperature encourages more extensive ring-opening polymerization and cross-linking, which limit chain mobility and improve the thermal stability of the resulting poly (NA-tz Bz). Overall, these FTIR, DSC, and TGA results consistently indicate that temperatures above 210 °C are essential to effectively initiate and complete the ring-opening polymerization of the NA-tz Bz monomer.

The stepwise curing protocol (150–270 °C) was intentionally employed to control the kinetics of the thermally triggered benzoxazine ring-opening polymerization and to avoid abrupt exothermic gelation, which can lead to inhomogeneous crosslinking and poor structural integrity. The progressive evolution of the FTIR spectra (Figs. 3a and 3d), where the characteristic oxazine-related vibrations gradually diminish and disappear at higher curing stages, confirms the continuous consumption of reactive oxazine units and network consolidation. In parallel, the DSC traces (Figs. 3b and 3e) show a marked decrease in the curing exotherm and reaction enthalpy after each heating stage, becoming nearly negligible after treatment at 240–270 °C, indicating a high conversion degree and near-complete polymerization. Consistently, the TGA profiles (Figs. 3c and 3f) reveal enhanced thermal resistance and increased char yields for the higher-temperature-cured samples, supporting the formation of a more condensed and thermally robust polymer framework. Collectively, these results justify the selected temperature program as an effective strategy for obtaining highly cross-linked, homogeneous polymer precursors suitable for subsequent carbonization.

3.3. Formation of C@poly (SA-tz Bz) and C@poly (NA-tz Bz) microporous carbons

The corresponding polybenzoxazines (poly (SA-tz Bz) and poly (NA-tz Bz)) were carbonized at 600 and 700 °C under a nitrogen atmosphere, without the use of activating agents, to produce N, O, and S co-doped microporous carbons (C@poly (SA-tz Bz 600), C@poly (NA-tz Bz 600), C@poly (SA-tz Bz 700), and C@poly (NA-tz Bz 700)). The carbonization yielded approximately 68 % for C@poly (SA-tz Bz 600), 76 % for C@poly (NA-tz Bz 600), 66 % for C@poly (SA-tz Bz 700) and 72 % for C@poly (NA-tz Bz 700) (Scheme 1b). We recorded FTIR spectra before and after carbonization to visualize the structural evolution from the polymer precursors to the carbon materials. As shown in Fig. S1, SA-tz Bz and NA-tz Bz at 270 °C display characteristic bands attributed to O–H/N–H stretching and vibrations associated with C═O, C═N, and C–S functionalities, confirming the presence of abundant polar groups in the polymer networks. After carbonization at 700 °C, these bands largely diminish or disappear, indicating the extensive decomposition/volatilization of the original functional groups, as well as the formation of a more carbon-rich framework. Meanwhile, the carbonized samples (C@poly (SA-tz Bz 700) and C@poly (NA-tz Bz 700)) show broad features consistent with increased aromatic/condensed carbon character (e.g., C═C skeletal vibrations and aromatic C–H bands). Overall, the FTIR measurement clearly illustrates the structural transformation from polar, functionalized polymers to carbonized, graphitic substances. The elimination of functional groups, coupled with the generation of aromatic carbon, is crucial for enhancing the material's stability and adsorption properties, particularly in CO_2 capture applications.

Fig. 4a and b, and S2 show the N_2 adsorption–desorption isotherms and the corresponding pore-size distributions of the N,O,S co-doped porous carbons derived from poly (SA-tz Bz) and poly (NA-tz Bz). All samples exhibit predominantly type-I isotherms, characterized by a sharp N_2 uptake at low relative pressures ($P/P_0 < 0.1$), which is typical of micropore-dominated structures. A slight additional uptake near $P/P_0 = 1.0$ can be attributed to interparticle voids and/or the presence of a small fraction of larger pores. The calculated Brunauer–Emmett–Teller (BET) surface areas are 154 ± 8 and 173 ± 12 $m^2\ g^{-1}$ for C@poly (SA-tz Bz 600) and C@poly (SA-tz Bz 700), respectively, while C@poly (NA-tz Bz 600) and C@poly (NA-tz Bz 700) show BET surface areas of 50 ± 11 and 165 ± 7 $m^2\ g^{-1}$, respectively, confirming the formation of porous carbon frameworks. The BET was measured three times for each carbon.

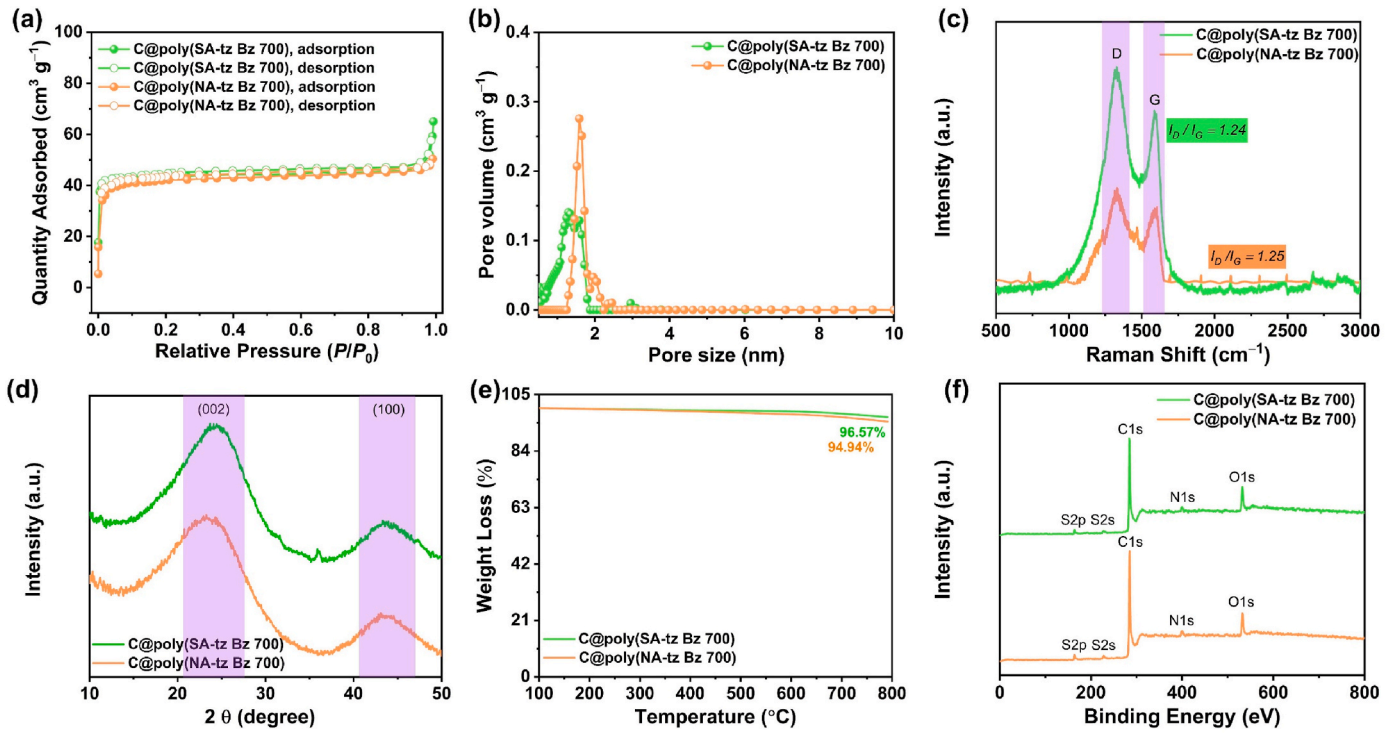

Fig. 4. (a) N_2 sorption isotherms, (b) pore size distributions, (c) Raman spectra, (d) XRD patterns, (e) TGA curves, and (f) XPS survey spectra of C@poly (SA-tz Bz 700) and C@poly (NA-tz Bz 700).

The higher surface area at 700 °C is attributed to more complete carbonization and aromatization, which promotes the removal of residual heteroatom-containing groups/volatile fragments and opens previously blocked micropores, thereby increasing accessible pore volume and N_2 uptake. In contrast, carbonization at 600 °C can leave partially carbonized fragments that occlude pore entrances, thereby reducing the accessible surface area. The pore size distribution profiles, derived from nonlocal density functional theory (NLDFT), show sharp peaks centered below 2 nm, further confirming the predominance of micropores in these materials. The narrow pore distributions and relatively high surface areas are expected to facilitate ion transport and charge storage, which are advantageous for electrochemical energy storage and gas adsorption applications. The Raman spectra of N, O, S co-doped microporous carbons materials identified by C@poly (SA-tz Bz 600), C@poly (SA-tz Bz 700), C@poly (NA-tz Bz 600), and C@poly (NA-tz Bz 700) (Fig. 4c and S3a) display two prominent peaks at approximately 1350 cm^{-1} (D band) and 1580 cm^{-1} (G band), which are characteristic of carbon-based materials [47,48]. The D band (A_{1g} mode) is associated with the presence of structural defects and disordered carbon domains, while the G band (E_{2g} mode) corresponds to the in-plane vibration of sp^2-hybridized carbon atoms in graphitic structures. Both samples show intense D bands, indicating a high density of defects, likely arising from the incorporation of heteroatoms (N, O, and S) into the carbon framework [49]. The degree of structural order was assessed using the intensity ratio (I_D/I_G) of the D and G bands, which were found to be 1.09 for C@poly (SA-tz Bz 600), 1.24 for C@poly (SA-tz Bz 700), 1.03 for C@poly (NA-tz Bz 600), and 1.25 for C@poly (NA-tz Bz 700). Remarkably, C@poly (SA-tz Bz 700) and C@poly (NA-tz Bz 700) show relatively high I_D/I_G values, confirming that both materials possess partially disordered graphitic carbon structures with abundant defect sites, which can be beneficial for enhancing electrochemical activity [50]. Further structural information was obtained from the XRD analysis of the carbonized samples. As shown in Fig. 4d and S3b, the XRD patterns of C@poly (SA-tz Bz 600), C@poly (SA-tz Bz 700), C@poly (NA-tz Bz 600), and C@poly (NA-tz Bz 700) exhibit two broad diffraction peaks centered at $2\theta \approx 24°$ and 44°, which can be assigned to the (002) and (100) reflections of turbostratic carbon, respectively. The broad (002) band indicates predominantly disordered/poorly stacked carbon layers, while the weak (100) reflection suggests partial development of in-plane aromatic carbon domains [51,52]. The interlayer spacing (d_{002}) calculated from the (002) reflection using Bragg's law ($d = \lambda/2\sin\theta$) is approximately 0.38 nm for C@poly (SA-tz Bz 600), 0.37 nm for C@poly (SA-tz Bz 700), 0.38 nm for C@poly (NA-tz Bz 600), and 0.36 nm for C@poly (NA-tz Bz 700). These values are slightly larger than crystalline graphite (0.34 nm), reflecting turbostratic disorder and the influence of heteroatom incorporation [53]. Notably, the 700 °C samples show a modest decrease in d_{002} compared with the 600 °C samples, consistent with slightly more compact stacking of carbon layers at higher carbonization temperature. In addition, the (100) peak at ~43.2° appears more intense in C@poly (NA-tz Bz 700) than in the other carbon materials, suggesting slightly more developed in-plane ordering/stacking in C@poly (NA-tz Bz 700), likely arising from its more condensed aromatic structure derived from the naphthalene-based precursor. Furthermore, we estimated the stacking height (Lc) from the (002) peak using the Scherrer equation ($Lc = K\lambda/\beta\cos\theta$). The calculated Lc values for C@poly (SA-tz Bz 600), C@poly (SA-tz Bz 700), C@poly (NA-tz Bz 600), and C@poly (NA-tz Bz 700) are 0.51, 0.65, 0.47, and 0.83 nm, respectively. The higher Lc values for the 700 °C samples suggest a modest increase in the stacking/ordering of aromatic carbon layers, with C@poly (NA-tz Bz 700) showing the largest Lc. Overall, these XRD results indicate only subtle differences among the samples and support a cautious interpretation of slightly improved structural ordering at higher carbonization temperature rather than a pronounced increase in graphitization. The thermogravimetric analysis profiles of C@poly (SA-tz Bz 600), C@poly (SA-tz Bz 700), C@poly (NA-tz Bz 600), and C@poly (NA-tz Bz 700) reveal their high thermal stability after carbonization (Fig. 4e and S3c). All carbon materials exhibit minimal weight loss (less than 10 %) even when heated up to 800 °C under a nitrogen atmosphere, indicating that the polymeric frameworks were successfully converted into highly stable carbon structures at carbonization temperatures of 600 and 700 °C. This remarkable thermal resistance reflects the formation of robust, cross-linked, and heteroatom-doped carbon networks, which are

advantageous for maintaining structural integrity during high-temperature electrochemical or gas adsorption applications. As shown in Fig. 4f and S3d, the surface elemental composition and chemical states of the carbon samples prepared at 600 and 700 °C, labeled C@poly (SA-tz Bz 600), C@poly (SA-tz Bz 700), C@poly (NA-tz Bz 600), and C@poly (NA-tz Bz 700), were investigated using X-ray photoelectron spectroscopy (XPS). The survey spectrum of C@poly (SA-tz Bz 600) reveals five characteristic peaks assigned to C 1s (283 eV), O 1s (530 eV), N 1s (399 eV), S 2s (227 eV), and S 2p (162 eV), whereas C@poly (SA-tz Bz 700) displays distinct peaks corresponding to C 1s (284 eV), O 1s (532 eV), N 1s (400 eV), S 2s (228 eV), and S 2p (164 eV). Additionally, C@poly (NA-tz Bz 600) was deconvoluted into five distinct peaks related to C 1s (284 eV), O 1s (532 eV), N 1s (398 eV), S 2s (229 eV), and S 2p (163 eV). Similarly, C@poly (NA-tz Bz 700) shows prominent peaks at C 1s (285 eV) and O 1s (532 eV), along with weaker but noticeable signals at N 1s (400 eV), S 2s (228 eV), and S 2p (165 eV). Confirming the successful incorporation of nitrogen, oxygen, and sulfur heteroatoms into the carbon framework. These results verify that these carbon materials are co-doped with N, O, and S, which is expected to enhance their electronic properties and surface reactivity. As shown in Fig. S4, high-resolution XPS deconvolution was performed to analyze the surface chemical composition and bonding states of the heteroatom-doped carbons. In the C 1s spectra, C@poly (SA-tz Bz 700) exhibits three prominent peaks at 284.38 eV (C═C/C–C/C–S), 285.42 eV (C–N/C–O), and 288.22 eV (C═O) (Fig. S4a), while C@poly (NA-tz Bz 700) shows corresponding peaks at 284.53, 285.57, and 288.37 eV, confirming similar carbon environments in both materials (Fig. S4e). The N 1s spectra of C@poly (SA-tz Bz 700) display four distinct components at 398.06 eV (pyridinic N), 399.24 eV (pyrrolic N), 400.26 eV (quaternary N), and 403.38 eV (oxidized N) (Fig. S4b); C@poly (NA-tz Bz 700) shows similar peaks at 398.13, 399.90, 401.10, and 402.30 eV, respectively (Fig. S4f). The O 1s spectra also reveal three types of oxygen species: for C@poly (SA-tz Bz), peaks at 531.12 eV (quinone-type), 532.66 eV (ether), and 535.16 eV (carboxyl) (Fig. S4c), and for C@poly (NA-tz Bz), at 531.6, 532.6, and 533.8 eV (Fig. S4g). Furthermore, the S 2p spectra of C@poly (SA-tz Bz 700) show two spin–orbit peaks at 163.64 eV (S $2p_{3/2}$) and 164.82 eV (S $2p_{1/2}$) with the expected 2:1 intensity ratio (Fig. S4d), which are also observed in C@poly (NA-tz Bz 700) at 163.79 eV and 164.97 eV (Fig. S4h). These results confirm the successful incorporation of N, O, and S heteroatoms in multiple bonding environments within both carbon frameworks. Heteroatom doping in microporous carbons is well known to enhance hydrophilicity, structural stability, specific capacitance, and overall electrochemical performance. As summarized in Table S3, the nitrogen functionalities in C@poly (SA-tz Bz 700) are composed of 15.22 % pyridinic N, 41.97 % pyrrolic N, 3.20 % quaternary N, and 39.61 % oxidized N, whereas C@poly (NA-tz Bz 700) contains 39.73 %, 23.84 %, 15.08 %, and 21.36 %, respectively. Quaternary N species are known to enhance redox activity, electronic conductivity, and charge transfer kinetics, while both pyridinic N and pyrrolic N functionalities contribute to improved electrochemical behavior by generating abundant defect sites, facilitating charge storage, and providing active centers [54]. These nitrogen groups also promote pseudocapacitive reactions, thereby increasing overall capacitance [55]. To establish a clearer structure–property relationship, the distribution of nitrogen species from XPS was correlated with the electrochemical kinetics and capacitance. As summarized in Table S3, the deconvoluted N 1s spectra show that C@poly (NA-tz Bz 700) contains a higher fraction of electrochemically active edge-type nitrogen (pyridinic + pyrrolic) than C@poly (SA-tz Bz 700) (N-6 + N-5 = 23.84 + 39.73 = 63.57 % compared to 41.97 + 15.22 = 57.19 %). The larger content of edge/defect-type N (pyridinic + pyrrolic) provides abundant redox-active sites and defective carbon domains that promote pseudocapacitive Faradaic reactions, thereby increasing the capacitance. Whereas quaternary N is generally linked to improved electronic conductivity and charge-transfer kinetics by integrating into the graphitic lattice. In addition, the presence of oxidized N (together with O/S species) enhances surface polarity and electrolyte wettability, which supports stable ion access to active sites during prolonged cycling. Regarding oxygen species, C@poly (SA-tz Bz 700) contains 52.93 % quinone-type O, 33.53 % ether O, and 13.54 % carboxylic O, while C@poly (NA-tz Bz 700) has 69.53 %, 15.80 %, and 14.67 %, respectively. These oxygen-containing groups can further enhance capacitance through reversible faradaic redox reactions [56]. In particular, acidic carboxyl groups can interact with hydroxyl ions in alkaline media, improving ion accessibility and charge transfer [57]. Therefore, the relatively higher nitrogen and oxygen contents in C@poly (NA-tz Bz 700) contribute to its superior specific capacitance and power density compared to C@poly (SA-tz Bz 700). Tables S4 and S5 show the theoretical and XPS-derived experimental atomic ratios (At%, excluding hydrogen) of C@poly (SA-tz Bz 600), C@poly (SA-tz Bz 700), C@poly (NA-tz Bz 600), and C@poly (NA-tz Bz 700) with sensitivity factor adjustment, demonstrating remarkable accordance that validates the suggested compositions. The theoretical ratios of C/N/O/S for all carbonized substituents nearly align with the observed values, validating that the synthesized carbon compounds preserve the anticipated framework and heteroatom functions. The robust theoretical-experimental agreement confirms the effective integration of the designed heteroatom contents into the carbon materials. The experimental heteroatom ratio (N, S, O) for C@poly (NA-tz Bz 700) is 19.20 %, surpassing the ratios of 13.87 %, 17.81 % and 16.60 % recorded for C@poly (SA-tz Bz 600), C@poly (SA-tz Bz 700), and C@poly (NA-tz Bz 600). This verifies that C@poly (NA-tz Bz 700) has the highest heteroatom content among the synthesized carbon compounds tested. Moreover, the bulk elemental composition of C@poly (SA-tz Bz 600), C@poly (SA-tz Bz 700), C@poly (NA-tz Bz 600), and C@poly (NA-tz Bz 700) was quantified by elemental analysis (Table S6) to complement the surface-sensitive XPS results. The elemental analysis confirms heteroatom incorporation in the carbon frameworks and shows that C@poly (NA-tz Bz 700) possesses the highest overall heteroatom content (N + S + O = 18.24 %), compared with 12.75 %, 16.99 %, and 15.80 % for C@poly (SA-tz Bz 600), C@poly (SA-tz Bz 700), and C@poly (NA-tz Bz 600), respectively. These bulk-composition trends are consistent with the XPS observations and provide a stronger basis for correlating heteroatom content with performance. We note that the improved electrochemical/CO_2 adsorption performance of C@poly (NA-tz Bz 700) is likely associated with its higher heteroatom content (enhanced polarity/active sites) together with its textural properties (e.g., microporosity and accessible surface area).

Fig. 5 and S5 present the microstructural and elemental characterization of the heteroatom-doped carbon materials C@poly (SA-tz Bz 600), C@poly (SA-tz Bz 700), C@poly (NA-tz Bz 600), and C@poly (NA-tz Bz 700). The TEM images of C@poly (SA-tz Bz 700) and C@poly (SA-tz Bz 600) (Fig. 5a and b and S5a and 5b) reveal thin, wrinkled, and loosely stacked carbon nanosheets with disordered domains, indicating the formation of amorphous microporous carbon structures after carbonization. In contrast, C@poly (NA-tz Bz 700) (Fig. 5h and i) exhibits thicker, more compact, and sheet-like structures, suggesting higher structural ordering derived from its naphthalene-based precursor. Whereas C@poly (NA-tz Bz 600) demonstrates a rod-like structure, as shown in Figs. S5c and S5d. The SEM images further confirm these morphological differences: C@poly (SA-tz Bz 700) (Fig. 5c) shows an aggregated, porous, and rough surface composed of irregular particles, while C@poly (NA-tz Bz 700) (Fig. 5j) displays smooth, dense, and well-defined sheet-like particles, consistent with enhanced graphitization. The SEM images further confirm these morphological differences: C@poly (SA-tz Bz 600) (Fig. S5e) shows relatively flat, plate-like/lamellar flake with smooth terraces and stacked layers, indicating a dense, sheet-like morphology with limited surface roughness, while C@poly (NA-tz Bz 600) (Fig. S5f) displays a highly crumpled and wrinkled “flower-like” aggregate composed of thin, folded rods, forming a 3D hierarchical structure with abundant edges, inter-sheet voids, and an overall rough surface. Fig. 5d–g, 5k-n, Figures S5h-k, and

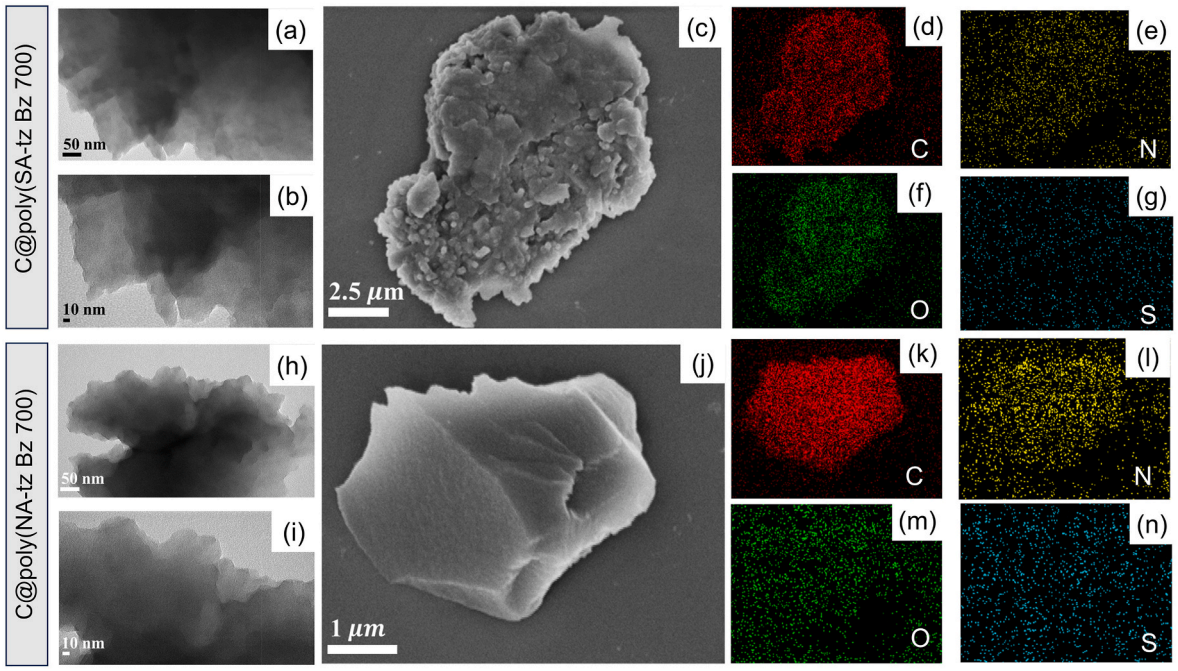

Fig. 5. (a,b) TEM and (c) SEM images of C@poly (SA-tz Bz 700); (d–g) SEM-EDS elemental maps of C, N, O, and S in C@poly (SA-tz Bz 700); (h,i) TEM and (j) SEM images of C@poly (NA-tz Bz 700); (k–n) SEM-EDS elemental maps of C, N, O, and S in C@poly (NA-tz Bz 700).

Figures S5m-p show the elemental EDS mapping of C@poly (SA-tz Bz 700), C@poly (NA-tz Bz 700), C@poly (SA-tz Bz 600), and C@poly (NA-tz Bz 600), respectively, demonstrating the homogeneous distribution of C, N, O, and S throughout the carbon frameworks and confirming successful heteroatom doping. The uniform dispersion of these elements is expected to enhance electronic conductivity, introduce abundant active sites, and improve the overall electrochemical performance of the materials.

3.4. Electrochemical properties of C@poly (SA-tz Bz 600), C@poly (SA-tz Bz 700), C@poly (NA-tz Bz 600), and C@poly (NA-tz Bz 700) microporous carbons

Electrochemical measurements were performed in a three-electrode configuration using 3 M KOH as the electrolyte. A carbon sheet served as the working electrode, a platinum wire as the counter electrode, and an Hg/HgO electrode as the reference. The electrochemical behaviors of the microporous carbons were evaluated through cyclic voltammetry

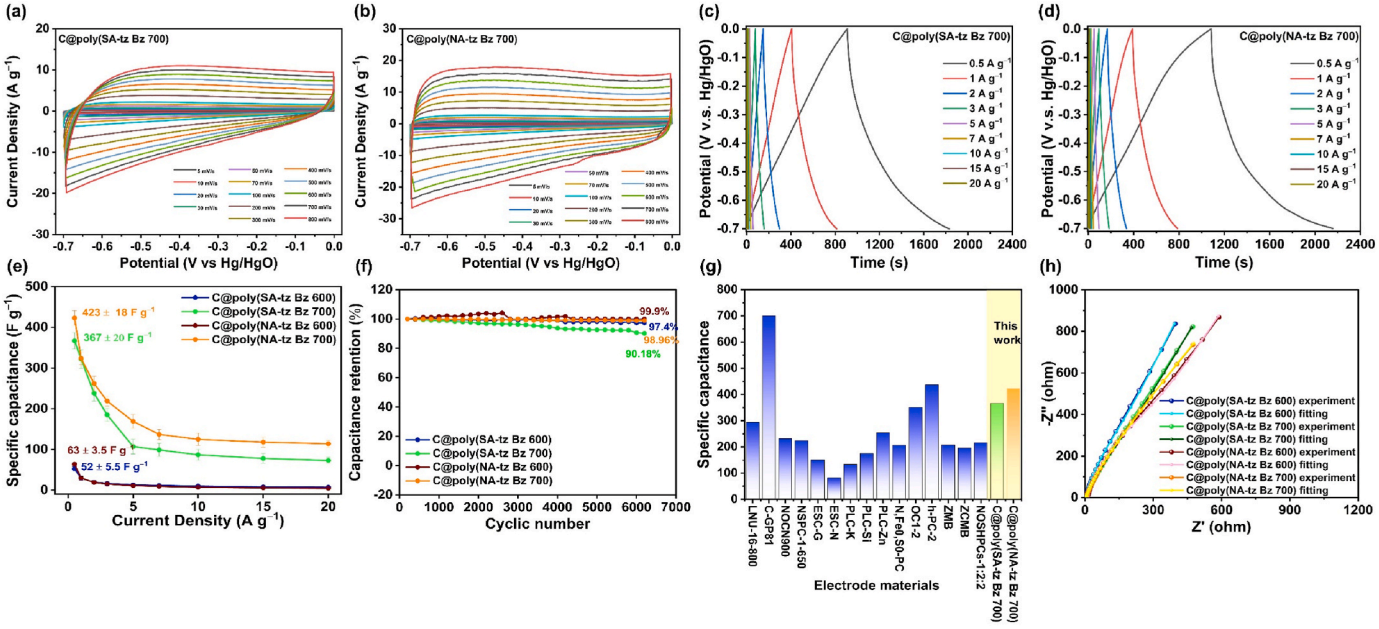

Fig. 6. (a,b) CV and (c,d) GCD profiles of C@poly (SA-tz Bz 700) and C@poly (NA-tz Bz 700) at various scan rates and current densities. (e) Specific capacitance at various current densities (n = 3), (f) Cycling stability at 10 A g^{-1}, (g) Comparison of the specific capacitance, and (h) the Nyquist plots and their corresponding fitted plots of C@poly (SA-tz Bz 600), C@poly (SA-tz Bz 700), C@poly (NA-tz Bz 600), and C@poly (NA-tz Bz 700).

(CV) and galvanostatic charge–discharge (GCD) tests over a potential window from −0.7 to 0.0 V. The CV curves of C@poly (SA-tz Bz 700), C@poly (NA-tz Bz 700), C@poly (SA-tz Bz 600), and C@poly (NA-tz Bz 600) were recorded at scan rates from 5 to 800 mV s^{-1} (−0.7–0.0 V vs. Hg/HgO), showing hallmarks of capacitive behavior (Fig. 6a and b, S6a, and S6b). The CV profiles retained their shape at high scan rate, highlighting the materials' exceptional stability, rapid charge–discharge kinetics, and robust EDLC performance [58,59]. A slight distortion/hump in the mid-negative region (≈−0.45 to −0.25 V) suggests additional pseudocapacitive contributions from surface redox of heteroatom sites (C–N/C–O/C–S) [56]. The enclosed CV area—and thus the current response—scales with scan rate for each material, with C@poly (NA-tz Bz 700) consistently enclosing a larger area than C@poly (SA-tz Bz 700), indicating higher capacitance and superior rate capability, consistent with its higher heteroatom content and defect density. Also, the unique morphology and optimized electron transport networks facilitated good electrolyte accessibility, as demonstrated by the consistent rise in current density without disruption of the CV shape at all scan rates [60,61]. Fig. 6c and d, S6c, and S6d show the GCD profiles of the C@poly (SA-tz Bz 700), C@poly (NA-tz Bz 700), C@poly (SA-tz Bz 600), and C@poly (NA-tz Bz 600) recorded at various current densities ranging from 0.5 to 20 A g^{-1}. The GCD curves manifested as triangular shapes with minimal curvature, thereby substantiating both pseudocapacitance and EDLC mechanisms for energy storage, consistent with the results derived from the CV measurements, attributed to the presence of heteroatoms [62–65]. C@poly (SA-tz Bz 700) (Fig. 6c) shows a shorter discharge time than C@poly (NA-tz Bz 700) (Fig. 6d), indicating a lower specific capacitance under the same testing conditions. Similarly, as shown in Fig. S6c and S6d, the 600 °C samples—C@poly (SA-tz Bz 600) and C@poly (NA-tz Bz 600)—exhibit shorter discharge durations than their 700 °C counterparts, suggesting reduced capacitance after carbonization at the lower temperature. The specific capacitances of the porous carbons were calculated from the GCD discharge curves using equation S (1). At a current density of 0.5 A g^{-1}, C@poly (SA-tz Bz 700) and C@poly (NA-tz Bz 700) deliver capacitances of 367 ± 20 and 423 ± 18 F g^{-1}, respectively (Fig. 6e). In comparison, the 600 °C samples exhibit much lower capacitances under the same conditions, with C@poly (SA-tz Bz 600) and C@poly (NA-tz Bz 600) showing 52 ± 5.5 and 63 ± 3.5 F g^{-1}, respectively (Fig. 6e). The number of repeated experiments at a current density of 0.5 A g−1 is three. The increased specific capacitance observed for C@poly (NA-tz Bz 700) microporous carbon is primarily attributed to the presence of high-heteroatom-doped carbon constituents and the relatively small pore size of the carbon. The nitrogen-containing entities (N-6 and N-5) in the carbon composites serve as electron donors, hence enhancing their whole capacitance. Prior studies have shown that the pore size of electrode materials significantly affects the efficiency of supercapacitors [66]. A decrease in pore size results in a shorter diffusion distance for electrolyte ions within the electrode structure during the charge-discharge cycle [67]. This accelerates ion movement and enhances charge storage efficiency, thereby improving the overall capacitance of the electrode. These findings suggest that the incorporation of heteroatoms and the control of porosity are crucial in determining the capacitance characteristics of multiple heteroatom-doped microporous carbons. Furthermore, we evaluated the reliability of our C@poly (SA-tz Bz 600), C@poly (SA-tz Bz 700), C@poly (NA-tz Bz 600), and C@poly (NA-tz Bz 700) microporous carbons-based electrodes by subjecting them to 6000 charge-discharge cycles at a current density of 10 A g^{-1}. Fig. 6f demonstrates that C@poly (SA-tz Bz 600), C@poly (SA-tz Bz 700), C@poly (NA-tz Bz 600), and C@poly (NA-tz Bz 700) exhibited good cycle stabilities, retaining 97.4 %, 90.18 %, 99.9 % and 98.96 % of their original specific capacitances, respectively. Remarkably, C@poly (SA-tz Bz 700) and C@poly (NA-tz Bz 700) exhibit enhanced electrochemical characteristics when compared to alternative doped carbon materials, as outlined in Fig. 6g and Table S7.

Electrochemical impedance spectroscopy (EIS) is commonly utilized to analyze the kinetics of charge storage in the fabricated electrode, specifically assessing the diffusion rate of ions and the resistivity of charge flow within the electrode. Fig. 6h presents the Nyquist plots of C@poly (SA-tz Bz 600), C@poly (SA-tz Bz 700), C@poly (NA-tz Bz 600), and C@poly (NA-tz Bz 700) measured over a frequency range from 0.01 Hz to 100 kHz with an AC amplitude of 5 mV. The microporous carbons show small semicircular arcs in the high-frequency region, reflecting low charge-transfer resistance and efficient ion transport at the electrode–electrolyte interface [68]. In the low-frequency region, the plots approach vertical lines, indicating good capacitive behavior and efficient ion diffusion within the porous structure [69]. To facilitate comparison, the intrinsic ohmic resistance (R_s)—which reflects the electrical conductivity of the microporous carbons—was determined from the intercept of the Z′ axis in the high-frequency region of the Nyquist plots. The R_s values of C@poly (SA-tz Bz 600), C@poly (SA-tz Bz 700), C@poly (NA-tz Bz 600), and C@poly (NA-tz Bz 700) were determined to be 4.56, 4.49, 11.96, and 4.26 Ω, respectively. The electrode based on C@poly (NA-tz Bz 700) showed better ion accessibility and lower charge-transfer resistance, as evidenced by its lower R_s value (Fig. 6h). Electrochemical impedance spectra were fitted using the equivalent circuit shown in Fig. S7, in which *R*s represents the series/ohmic resistance (electrolyte resistance, intrinsic electrode resistance, and contact resistance), while two interfacial processes are described by *R*ct1‖CPE1 and *R*ct2‖CPE2. Here, *R*ct1 with CPE1 accounts for the high-to-mid frequency charge-transfer response at the electrode/electrolyte interface (non-ideal capacitive behavior arising from surface heterogeneity), whereas *R*ct2 with CPE2 reflects a slower process at lower frequencies, commonly associated with charge transfer/ion transport in the porous carbon network and within micropores. Based on the fitted EIS parameters in Table S8, a clear comparison can be made by grouping the samples by carbonization temperature. At 700 °C, both carbons show low solution resistance (*R*s), but C@poly (NA-tz Bz 700) delivers the most favorable kinetics overall (*R*s = 4.12 Ω, *R*ct1 = 197.3 Ω, *R*ct2 = 5209 Ω). In comparison, C@poly (SA-tz Bz 700) has a similar ohmic resistance (*R*s = 4.48 Ω) and slightly higher interfacial charge-transfer resistance (*R*ct1 = 211.3 Ω), yet a much larger low-frequency resistance (*R*ct2 = 12,014 Ω), suggesting more hindered ion transport and/or slower processes within the porous electrode (e.g., diffusion through micropores). This improved kinetic behavior of C@poly (NA-tz Bz 700) correlates well with its higher fraction of quaternary N (15.08 %), which favors charge transfer and electrical transport, together with a high proportion of pyridinic/pyrrolic N that provides redox-active sites, explaining its higher specific capacitance (423 F g^{-1} at 0.5 A g^{-1}) compared with C@poly (SA-tz Bz 700) (367 F g^{-1} at 0.5 A g^{-1}). Moreover, the robust cycling retention of C@poly (NA-tz Bz 700) (98.96 % after 6000 cycles) can be rationalized by the combined effects of conductive/graphitic N functionalities, as well as polar heteroatom functionalities, which improve wettability and stabilize reversible surface redox reactions during repeated cycling. At 600 °C, C@poly (SA-tz Bz 600) shows a low *R*s (4.59 Ω) but relatively high resistances associated with charge transfer/transport (*R*ct1 = 245.2 Ω, *R*ct2 = 7610 Ω). In contrast, C@poly (NA-tz Bz 600) exhibits a markedly higher *R*s (11.79 Ω) together with the largest *R*ct1 (382.6 Ω), indicating poorer electrode/electrolyte contact and slower interfacial charge transfer, although its *R*ct2 (6094 Ω) is somewhat lower than that of SA-tz Bz 600. Overall, comparing 700 °C vs 600 °C reveals that increasing the carbonization temperature generally reduces resistive losses and improves electrochemical kinetics, most notably for the naphthalene-derived carbon (NA-tz Bz 700), which combines the lowest *R*s and *R*ct1 with the smallest *R*ct2, consistent with more efficient ion/electron transport during charge–discharge. These results indicate that the carbons exhibiting the highest conductivity, elevated heteroatom concentration, and reduced pore size demonstrate enhanced performance. Thus, the synthesized carbons exhibit significant potential as candidate materials for energy storage applications. The Bode magnitude plots in Fig. S8a reveal sloped lines with negative gradients at low frequencies, reflecting

low resistance, and flat regions at high frequencies, indicating strong capacitive behavior. Fig. S8b displays the phase angle plots, where the knee frequencies—defined at a phase angle of −45°—mark the transition point between resistive and capacitive dominance, indicating the rate capability. The knee frequencies for C@poly (SA-tz Bz 700) and C@poly (NA-tz Bz 700) are 0.13296 ms and 0.11192 ms, respectively, confirming their good charge transport properties. Furthermore, the electrical conductivity of the carbon materials was measured at room temperature using a four-probe method. C@poly (SA-tz Bz 600), C@poly (SA-tz Bz 700), C@poly (NA-tz Bz 600), and C@poly (NA-tz Bz 700) show conductivities of 23.36, 28.19, 9.24, and 30.33 S cm^{-1}, respectively. Overall, the higher conductivities, especially for the 700 °C samples, indicate more efficient electron transport, which is consistent with the formation of a more ordered, condensed carbon framework (i.e., improved structural ordering/graphitic-like domains) after carbonization at the higher temperature.

Carbonization at 700 °C leads to markedly higher capacitance than at 600 °C (e.g., 367 and 423 F g^{-1} for C@poly (SA-tz Bz 700) and C@poly (NA-tz Bz 700) vs. 52.3 and 63.4 F g^{-1} for C@poly (SA-tz Bz 600) and C@poly (NA-tz Bz 700) at 0.5 A g^{-1}), indicating that the higher temperature produces a carbon framework with more favorable charge-storage/transport characteristics. This improvement is consistent with the textural and structural evolution: the BET surface area increases from 154 ± 8 to 173 ± 12 m^2 g^{-1} for SA-tz Bz-based carbons and more strongly from 50 ± 11 to 165 ± 7 m^2 g^{-1} for NA-tz Bz-based carbons when increasing the carbonization temperature from 600 to 700 °C, suggesting that more complete carbonization at 700 °C opens previously blocked micropores and increases accessible surface area for ion adsorption. In parallel, XRD shows slightly more compact/ordered carbon stacking at 700 °C, evidenced by the modest decrease in d_{002} and the increased stacking height (Lc) (e.g., Lc = 0.65 and 0.83 nm for C@poly (SA-tz Bz 700) and C@poly (NA-tz Bz 700) vs. 0.51 and 0.47 nm for C@poly (SA-tz Bz 600) and C@poly (NA-tz Bz 600)), supporting improved aromatic layer stacking that benefits electrical transport. Importantly, the 700 °C carbons also retain a higher density of surface heteroatoms (total N + O + S from XPS: 17.81 at% for C@poly (SA-tz Bz 700) and 19.20 at% for C@poly (NA-tz Bz 700) vs. 13.87 at% for C@poly (SA-tz Bz 600) and 16.60 at% for C@poly (NA-tz Bz 600)), providing more redox-active sites and wettability/defect sites that contribute to pseudocapacitance. This trend is consistent with bulk elemental analysis, which shows that the total heteroatoms (N + S + O) are 16.99 % for C@poly (SA-tz Bz 700) and 18.24 % for C@poly (NA-tz Bz 700), compared to 12.75 % for C@poly (SA-tz Bz 600) and 15.80 % for C@poly (NA-tz Bz 600). Finally, EIS fitting supports faster interfacial kinetics after carbonization at 700 °C—most notably for C@poly (NA-tz Bz 700), which shows the lowest overall resistances (Rs = 4.12 Ω, $Rct1$ = 197.3 Ω, $Rct2$ = 5209 Ω), indicating more favorable ion/electron transport and reduced polarization compared with the 600 °C samples (e.g., C@poly (NA-tz Bz 600): Rs = 11.79 Ω, $Rct1$ = 382.6 Ω). Overall, the higher capacitance of the 700 °C carbons arises from a synergistic balance of (i) higher accessible porosity, (ii) slightly improved carbon-layer stacking/ordering, and (iii) higher heteroatom density; within the 700 °C series, C@poly (NA-tz Bz 700) surpasses C@poly (SA-tz Bz 700) primarily because it combines the highest heteroatom content with the most favorable impedance characteristics, consistent with more efficient charge transfer and ion transport in the electrode.

Between the two 700 °C carbons, C@poly (NA-tz Bz 700) delivers a higher capacitance than C@poly (SA-tz Bz 700) because it combines more efficient charge/ion transport with a higher density of heteroatom-derived active sites. From EIS fitting (Table S8), C@poly (NA-tz Bz 700) shows the lowest overall resistances (Rs = 4.12 Ω, $Rct1$ = 197.3 Ω, $Rct2$ = 5209 Ω), whereas C@poly (SA-tz Bz 700), despite having comparable Rs (4.48 Ω) and $Rct1$ (211.3 Ω), exhibits a much larger low-frequency resistance ($Rct2$ = 12,014 Ω), implying more hindered ion transport within the porous electrode (e.g., diffusion in micropores). Structurally, XRD indicates slightly improved carbon-layer stacking/ordering for C@poly (NA-tz Bz 700), with a larger stacking height and smaller interlayer spacing (Lc = 0.83 nm and d_{002} = 0.36 nm) compared with C@poly (SA-tz Bz 700) (Lc = 0.65 nm and d_{002} = 0.37 nm), which supports more effective electron transport; this is consistent with its higher electrical conductivity (30.33 vs 28.19 S cm^{-1}). In addition, XPS/elemental analysis shows that C@poly (NA-tz Bz 700) retains the highest total heteroatom content (N + O + S), providing more polar/redox-active sites that enhance wettability and contribute additional pseudocapacitance in alkaline electrolyte. Overall, the combination of lower impedance, slightly higher structural ordering, and higher heteroatom content explains why C@poly (NA-tz Bz 700) achieves the best capacitance among the prepared carbons under identical testing conditions.

Finally, these results indicate that 700 °C provides a practical compromise between electronic conductivity and framework preservation. At this temperature, the carbon framework becomes sufficiently condensed to improve charge transport, while excessive graphitization is avoided so that N-, S-, and O-containing functionalities are still retained. In addition, a substantial level of microporosity is preserved, maintaining abundant ion-accessible sites for charge storage. Therefore, carbonization at 700 °C yields heteroatom-rich porous carbons with favorable transport properties and strong electrochemical performance, supporting its selection in this work.

3.5. Two electrodes symmetric supercapacitor device

Inspired by the high performance demonstrated in the three-electrode system, we evaluated the practical applicability of C@poly (NA-tz Bz 700) by developing a symmetric supercapacitor (SC) device with a two-electrode setup (Fig. 7a). The device was assembled using 3 M KOH as the electrolyte and filter paper as the separator placed between two C@poly (NA-tz Bz 700)-based electrodes. Fig. 7b shows the CV profiles of the C@poly (NA-tz Bz 700)-based symmetric supercapacitor measured at scan rates ranging from 3 to 80 mV s^{-1} within a potential window of 0.0–1.6 V. The CV curves exhibit a nearly rectangular shape with slight distortion at higher scan rates, which is characteristic of electric double-layer capacitor (EDLC)-type behavior combined with minor pseudocapacitive contributions. The well-retained shape even at high scan rates indicates good rate capability and rapid charge–discharge kinetics, as the electrode can maintain fast ion adsorption/desorption without significant polarization. The broad humps visible in the mid-potential region suggest faradaic redox reactions from heteroatom (N, O, S) active sites, which contribute to additional pseudocapacitance. The progressive increase in enclosed areas with rising scan rate demonstrates the material's ability to deliver higher current responses and sustain fast charge storage, confirming its suitability for high-power supercapacitor applications. Fig. 7c shows the GCD profiles of the C@poly (NA-tz Bz 700)-based symmetric device recorded at current densities from 0.5 to 8 A g^{-1} within a potential window of 0–1.4 V. All GCD curves exhibit nearly triangular shapes with minimal IR drop, indicating high Coulombic efficiency, low internal resistance, and good reversibility during charge–discharge cycling. The specific capacitance values calculated from the GCD curves using Equation S(2) (Fig. 7d) decrease from 342 F g^{-1} at 0.5 A g^{-1} to 75 F g^{-1} at 8 A g^{-1}, reflecting the expected decline in capacitance at higher current loads. These high capacitance values, especially at low current densities, highlight the high charge storage capability of the electrode and surpass many previously reported symmetric and asymmetric supercapacitors based on similar redox-active carbon materials (39–357 F g^{-1}, Table S9), demonstrating the superior electrochemical performance of the C@poly (NA-tz Bz)-based device. The EIS results (Fig. 7e) show a small semicircle in the high-frequency region that transitions into a nearly vertical line at low frequencies, indicating low charge-transfer resistance and ideal capacitive behavior. Ragone plot (Fig. S9) illustrates the relationship between energy density and power density of the C@poly (NA-tz Bz 700)-based symmetric supercapacitor, highlighting its high energy storage capability across a broad range of

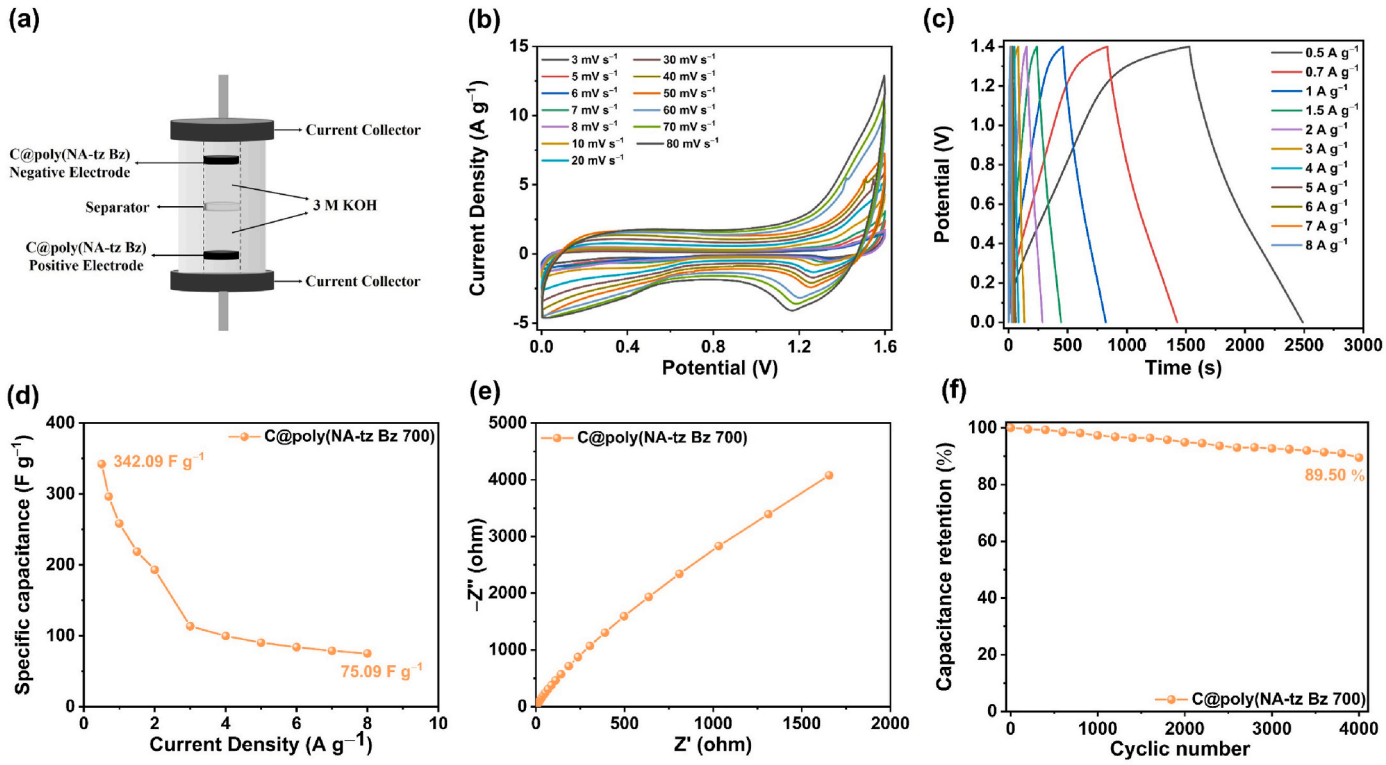

Fig. 7. (a) Schematic illustration of the device configuration. (b) CV curves, (c) GCD curves, (d) specific capacitance, (e) EIS, and (f) cycling stability of the C@poly (NA-tz Bz 700)-based SC device.

operating conditions. The device delivers a maximum energy density of 93.12 Wh kg^{-1} at a power density of around 349 W kg^{-1}, which is significantly higher than typical values reported for conventional carbon-based supercapacitors. As the power density increases, the energy density gradually decreases due to shorter charge–discharge times and reduced utilization of active sites at higher current loads, yet the device still maintains ~20 Wh kg^{-1} even at an ultrahigh power density of ~5590 W kg^{-1}, demonstrating high-rate performance. This favorable balance between high energy and high-power densities can be attributed to the synergistic effect of the microporous structure and abundant N, O, and S heteroatom doping in C@poly (NA-tz Bz 700), which provides rapid ion transport pathways, high charge storage capacity, and additional pseudocapacitive contributions. As shown in Fig. 7f, the C@poly (NA-tz Bz 700)-based supercapacitor retains 89.5 % of its initial capacitance after 4000 charge–discharge cycles at 0.5 A g^{-1}, confirming its good cycling stability and rate performance.

3.6. CO_2 capture

Energy storage and CO_2 adsorption, though seemingly distinct applications, are closely interrelated when employing materials such as N, O, and S co-doped microporous carbons. Both functions rely on key structural features, including high surface area, abundant microporosity, and tailored surface chemistry. These carbonaceous materials offer synergistic advantages: their microporous porosity facilitates rapid ion transport in supercapacitors and enhances CO_2 diffusion and uptake, while heteroatom doping (e.g., nitrogen, oxygen, sulfur) introduces redox-active sites and increases the affinity for CO_2 molecules [70]. Their robust conjugated frameworks contribute to electrochemical stability and strengthen CO_2 interactions through π–π stacking and electrostatic forces. These shared characteristics make N, O, and S co-doped microporous carbons versatile candidates capable of addressing both energy storage and carbon dioxide capture simultaneously. Enhancing CO_2-philic surface properties and maximizing surface area are critical for achieving superior CO_2 adsorption performance. In addition, the incorporation of heteroatoms such as nitrogen, oxygen, and sulfur into the carbon framework introduces polar surface sites that enhance electrostatic interactions with CO_2. These heteroatom sites interact with the quadrupole moment of CO_2 molecules through dipole–quadrupole forces and Lewis acid–base interactions, thereby significantly enhancing the CO_2 affinity of the porous carbon matrix [71]. The CO_2 adsorption performance of the synthesized N, O, and S co-doped porous carbons was evaluated at 273 K and 298 K under 1.0 bar, as shown in Fig. 8 and summarized in Table S10. At 298 K, C@poly (SA-tz Bz 600), C@poly (SA-tz Bz 700), C@poly (NA-tz Bz 600), and C@poly (NA-tz Bz 700) exhibit CO_2 adsorption capacities of 46.09, 59.94, 17.41, and 119.00 $cm^3\ g^{-1}$, respectively. Upon decreasing the temperature to 273 K, the adsorption capacities increase markedly to 105.73, 127.95, 48.46, and 231.69 $cm^3\ g^{-1}$, respectively, indicating enhanced CO_2 uptake at lower temperatures. In addition, we calculated the isosteric heat of adsorption (*Q*st) from the CO_2 isotherms at 273 and 298 K using the Clausius–-Clapeyron approach. The obtained *Q*st values are approximately 59, 72, 48, and 34 kJ mol^{-1} for C@poly (SA-tz Bz 700), C@poly (NA-tz Bz 700), C@poly (SA-tz Bz 600), and C@poly (NA-tz Bz 600), respectively. This marked enhancement confirms the strong affinity of these heteroatom-doped microporous carbons for CO_2 at lower temperatures. As highlighted in Table S10, the CO_2 uptake of C@poly (NA-tz Bz 700) is among the highest reported for heteroatom-doped porous carbons, exceeding the typical ranges of 44.58–157.7 $cm^3\ g^{-1}$ at 273 K observed for similar N/O-doped microporous carbons [72,73]. This superior performance is attributed to its more extended aromatic framework, which forms a denser and better-interconnected microporous network, and its higher retention of nitrogen, oxygen, and sulfur functionalities, which create abundant polar sites for CO_2 adsorption.

C@poly (NA-tz Bz 700) exhibits the highest CO_2 uptake (119.00 $cm^3\ g^{-1}$ at 298 K and 231.69 $cm^3\ g^{-1}$ at 273 K) because it combines the richest polar surface chemistry with a more favorable microporous adsorption environment. Elemental analysis confirms that C@poly (NA-

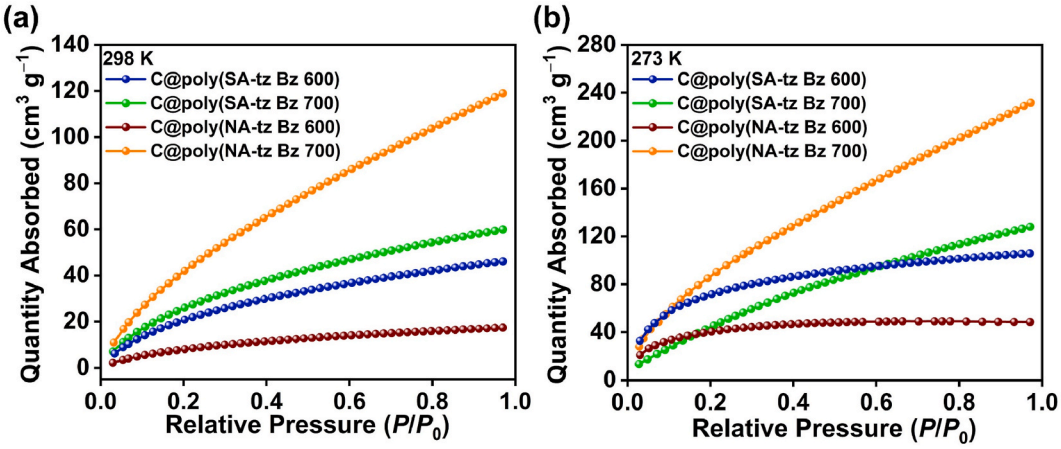

Fig. 8. (a,b) CO_2 capture of C@poly (SA-tz Bz 600), C@poly (SA-tz Bz 700), C@poly (NA-tz Bz 600), and C@poly (NA-tz Bz 700) under 298 and 273 K.

tz Bz 700) retains the highest overall heteroatom content (N + O + S = 18.24 %), exceeding C@poly (SA-tz Bz 600) (12.75 %), C@poly (SA-tz Bz 700) (16.99 %), and C@poly (NA-tz Bz 600) (15.80 %). The higher density of N/O/S functionalities introduces abundant polar adsorption sites that strengthen CO_2–surface interactions through dipole–quadrupole interactions and Lewis acid–base-type binding, which becomes more pronounced at lower temperature—consistent with the marked increase in uptake from 298 to 273 K. In addition, the naphthalene-derived precursor promotes a more extended aromatic carbon backbone after carbonization, which can generate a denser and better-interconnected microporous network, thereby improve the CO_2-accessible pore volume and facilitating diffusion into adsorption sites. By contrast, the lower CO_2 uptakes of C@poly (SA-tz Bz 600), C@poly (SA-tz Bz 700), and C@poly (NA-tz Bz 600) can be attributed to their lower heteroatom contents and/or less optimal microporous connectivity, resulting in fewer and weaker CO_2 binding sites and reduced adsorption capacity.

In addition, the pore-size distribution analysis highlights that CO_2 uptake is strongly governed by the accessible micropore volume and the dominant micropore width rather than the BET surface area alone. At 700 °C, C@poly (NA-tz Bz 700) shows a higher micropore volume (0.275 $cm^3\ g^{-1}$) with a dominant pore size of ~1.6 nm, whereas C@poly (SA-tz Bz 700) exhibits a smaller micropore volume (0.140 $cm^3\ g^{-1}$) centered at ~1.3 nm. This larger micropore volume in C@poly (NA-tz Bz 700) provides a greater number of CO_2-accessible adsorption sites and enables more efficient pore filling, which correlates well with its substantially higher CO_2 uptake (119.00 $cm^3\ g^{-1}$ at 298 K and 231.69 $cm^3\ g^{-1}$ at 273 K). In contrast, for the 600 °C carbons, although C@poly (SA-tz Bz 600) has a relatively higher micropore volume (0.222 $cm^3\ g^{-1}$, ~1.21 nm) than C@poly (NA-tz Bz 600) (0.115 $cm^3\ g^{-1}$, ~1.23 nm), both materials show markedly lower CO_2 capacities overall, indicating that pore volume alone is not sufficient at the lower carbonization temperature. This behavior is consistent with the idea that the superior adsorption of C@poly (NA-tz Bz 700) arises from a synergistic combination of (i) a better-developed microporous network (higher micropore volume) and (ii) a higher density of polar N/O/S functionalities that strengthen CO_2–surface interactions; therefore, both textural confinement and chemical affinity contribute to the observed enhancement in CO_2 capture.

To assess whether the carbon frameworks remain stable during CO_2 capture, we examined C@poly (SA-tz Bz 700) and C@poly (NA-tz Bz 700) before and after CO_2 adsorption using FTIR and TGA (Fig. S10a–d). The FTIR spectra show only minor changes after adsorption (Fig. S10a and b), indicating that CO_2 is mainly taken up through reversible physisorption (weak interactions with polar surface sites) rather than formation of new covalent bonds, and that the chemical structure of the carbons is largely preserved. Consistently, TGA profiles reveal that both materials maintain high thermal stability after CO_2 exposure (Fig. S10c and d): C@poly (SA-tz Bz 700) and C@poly (NA-tz Bz 700) retain 90.30 % and 88.54 % of their mass, respectively, at 800 °C, demonstrating negligible degradation. Overall, the essentially unchanged FTIR features together with the strong post-adsorption thermal stability confirm that these carbons possess robust structural integrity and are suitable for repeated/extended CO_2 adsorption without significant framework deterioration.

4. Conclusions

In this work, we developed a sustainable and straightforward strategy for synthesizing two novel heterocyclic Schiff base–derived benzoxazine monomers, SA-tz Bz and NA-tz Bz, which were converted via thermal ring-opening polymerization followed by direct carbonization into N, O, and S co-doped microporous carbons (C@poly (SA-tz Bz) and C@poly (NA-tz Bz)). The chemical structures of the monomers were confirmed by ^1H and ^{13}C NMR, FTIR, DSC, and TGA analyses. FTIR, DSC, and TGA revealed that the optimal curing temperature for benzoxazine ring-opening and polymer network formation was above 210 °C, enabling efficient conversion into cross-linked polybenzoxazines. The cross-linked poly (SA-tz Bz) and poly (NA-tz Bz) were then carbonized separately at 600 and 700 °C for 6 h under a nitrogen atmosphere to produce C@poly (SA-tz Bz 600), C@poly (SA-tz Bz 700), C@poly (NA-tz Bz 600) and C@poly (NA-tz Bz 700). This approach avoids the use of activating agents or toxic reagents and yielded carbon materials with high surface areas (up to 173), hierarchical microporosity, and abundant heteroatom (N, O, S) functionalities. Among the carbons, C@poly (NA-tz Bz 700) exhibited superior electrochemical performance, achieving a specific capacitance of 423 ± 18 F g^{-1} at 0.5 A g^{-1}, good cycling stability (98 % retention after 6000 cycles), and high rate capability (342 F g^{-1} in a symmetric device with 89.50 % retention after 4000 cycles). Moreover, it delivered an exceptional CO_2 adsorption capacity of 231.7 $cm^3\ g^{-1}$ at 273 K and 119.0 $cm^3\ g^{-1}$ at 298 K, far exceeding C@poly (SA-tz Bz 700) (127.95 and 59.9 $cm^3\ g^{-1}$, respectively) and many reported heteroatom-doped porous carbons. These superior properties are attributed to the synergistic effects of a higher heteroatom content, which enhances redox activity, electrical conductivity, ion accessibility, and CO_2 affinity through dipole–quadrupole and Lewis acid–base interactions. Overall, this study establishes benzothiazole-based polybenzoxazines as a versatile precursor platform for producing multifunctional heteroatom-doped carbons that combine high-performance energy storage with efficient CO_2 capture, offering great potential for next-generation electrochemical and carbon capture applications.

CRediT authorship contribution statement

Yun-Chien Zheng: Writing – original draft, Validation, Resources, Methodology, Formal analysis, Data curation. **Shimaa Abdelnaser:** Writing – original draft, Validation, Software, Methodology, Investigation, Conceptualization. **Yousra M. Nabil:** Methodology, Investigation, Conceptualization. **Mostafa Sayed:** Visualization, Methodology. **Shiao-Wei Kuo:** Project administration, Investigation, Funding acquisition. **Chih-Feng Wang:** Validation, Supervision, Formal analysis. **Mostafa Ahmed:** Validation, Resources, Methodology. **Ahmed F.M. EL-Mahdy:** Writing – review & editing, Writing – original draft, Validation, Supervision, Software, Data curation, Conceptualization.

Declaration of competing interest

The authors declare that they have no known competing financial interests or personal relationships that could have appeared to influence the work reported in this paper.

Acknowledgments

This study was supported financially by the National Science and Technology Council, Taiwan, under contract NSTC 112-2221-E-110-005-MY3, and the Central Department of Missions, Ministry of Higher Education and Scientific Research, Egypt. Professor Mostafa Ahmed gratefully acknowledges Prof. Dr. De-Qi Yuan and Dr. Tatsuya Takimoto for providing chemicals, facilitating NMR measurements, and offering valuable support during the scientific visit to the Faculty of Pharmacy, Kobe Gakuin University, Japan. Special thanks are extended to Honoka Kitano, a fifth-year student, for her kind assistance.

Appendix A. Supplementary data

Supplementary data to this article can be found online at https://doi.org/10.1016/j.polymer.2026.129674.

Data availability

Data will be made available on request.

References

[1] N.N. Loganathan, V. Perumal, B.R. Pandian, R. Atchudan, T. Edison, M. Ovinis, Recent studies on polymeric materials for supercapacitor development, J. Energy Storage 49 (2022) 22.
[2] H.X. Li, M.H. Tang, L. Wang, Q. Liu, F. Yao, Z.Y. Gong, Y.C. Li, S.Y. Lu, J.H. Yan, Molecular simulation combined with DFT calculation guided heteroatom-doped biochar rational design for highly selective and efficient CO_2 capture, Chem. Eng. J. 481 (2024) 11.
[3] Z. Liu, Z. Deng, S.J. Davis, C. Giron, P. Ciais, Monitoring global carbon emissions in 2021, Nat. Rev. Earth Environ. 3 (2022) 217–219.
[4] J.L. Bai, J.W. Shao, Q.Y. Yu, M. Demir, B.N. Altay, T.M. Ali, Y.F. Jiang, L.L. Wang, X. Hu, Sulfur-doped porous carbon adsorbent: a promising solution for effective and selective CO2 capture, Chem. Eng. J. 479 (2024) 8.
[5] T.Y. Lu, J.L. Bai, M. Demir, X. Hu, J.M. Huang, L.L. Wang, Synthesis of potassium Bitartrate-derived porous carbon via a facile and Self-Activating strategy for CO_2 adsorption application, Sep. Purif. Technol. 296 (2022) 8.
[6] W.J. Wu, C.L. Wu, J. Liu, H.Y. Yan, G.Q. Li, Y.Q. Zhao, K.L. Bei, G.J. Zhang, Synergistic effects of heteroatom doping and narrow micropores on carbon dioxide capture in bamboo shoot shell-based porous carbon, Sep. Purif. Technol. 339 (2024) 14.
[7] B. Petrovic, M. Gorbounov, S.M. Soltani, Influence of surface modification on selective CO_2 adsorption: a technical review on mechanisms and methods, Microporous Mesoporous Mater. 312 (2021) 41.
[8] B. Petrovic, M. Gorbounov, S.M. Soltani, Impact of surface functional groups and their introduction methods on the mechanisms of CO2 adsorption on porous carbonaceous adsorbents, Carbon Capture Sci. Technol. 3 (2022) 100045.
[9] H.Y. Kong, T.X. Wang, Y. Tao, X.S. Ding, B.H. Han, Crown ether-based hypercrosslinked porous polymers for gold adsorption, Sep. Purif. Technol. 290 (2022) 10.
[10] A.A. Alhwaige, H. Ishida, S.A. Qutubuddin, Nitrogen-enriched carbon aerogels derived from polybenzoxazine cross-linked graphene oxide-chitosan hybrid matrix with superior CO2 capture performance, ACS Applied Engineering Materials 2 (2024) 1672–1686.
[11] I. Tiwari, P. Sharma, L. Nebhani, Polybenzoxazine- an enticing precursor for engineering heteroatom- doped porous carbon materials with applications beyond energy, environment and catalysis, Mater. Today Chem. 23 (2022) 49.
[12] C.D. Ma, J.L. Bai, M. Demir, X. Hu, S.F. Liu, L.L. Wang, Water chestnut shell-derived N/S-doped porous carbons and their applications in CO2 adsorption and supercapacitor, Fuel 326 (2022) 12.
[13] J.L. Bai, J.M. Huang, Q.Y. Yu, M. Demir, F.H. Gecit, B.N. Altay, L.L. Wang, X. Hu, One-pot synthesis of self S-doped porous carbon for efficient CO2 adsorption, Fuel Process. Technol. 244 (2023) 9.
[14] X.F. Yuan, J.F. Xiao, M. Yilmaz, T.C. Zhang, S.J.N. Yuan, P Co-doped porous biochar derived from cornstalk for high performance CO2 adsorption and electrochemical energy storage, Sep. Purif. Technol. 299 (2022) 13.
[15] X.Y. Qian, L. Miao, J.X. Jiang, G.C. Ping, W. Xiong, Y.K. Lv, Y.F. Liu, L.H. Gan, D. Z. Zhua, M.X. Liu, Hydrangea -like N/O codoped porous carbons for high-energy supercapacitors, Chem. Eng. J. 388 (2020) 10.
[16] J.Y. Wang, Y.L. Xu, M.F. Yan, B. Ren, X.X. Dong, J.F. Miao, L.H. Zhang, X.Q. Zhao, Z.F. Liu, Preparation and application of biomass-based porous carbon with S, N, Zn, and Fe heteroatoms loading for use in supercapacitors, Biomass Bioenergy 156 (2022) 13.
[17] M.G. Mohamed, M.Y. Tsai, W.C. Su, A.F.M. EL-Mahdy, C.F. Wang, C.F. Huang, L. Dai, T. Chen, S.W. Kuo, Nitrogen-doped microporous carbons derived from azobenzene and nitrile-functionalized polybenzoxazines for CO_2 uptake, Mater. Today Commun. 24 (2020) 101111.
[18] U. Kamran, S.J. Park, Chemically modified carbonaceous adsorbents for enhanced CO2 capture: a review, J. Clean. Prod. 290 (2021) 26.
[19] W.L. Shi, X.F. Zhao, S.X. Ren, W.Z. Li, Q.H. Zhang, X.D. Jia, Heteroatoms co-doped porous carbons from amino acid based polybenzoxazine for superior CO2 adsorption and electrochemical performances, Eur. Polym. J. 165 (2022) 14.
[20] E. Dhandapani, S. Thangarasu, S. Ramesh, K. Ramesh, R. Vasudevan, N. Duraisamy, Recent development and prospective of carbonaceous material, conducting polymer and their composite electrode materials for supercapacitor-A review, J. Energy Storage 52 (2022) 35.
[21] S.H. An, C.B. Lu, Q. Xu, C. Lian, C.J. Peng, J. Hu, X.D. Zhuang, H.L. Liu, Constructing catalytic crown ether-based covalent organic frameworks for electroreduction of CO2, ACS Energy Lett. 6 (2021) 3496–3502.
[22] S. Sardana, A. Gupta, K. Singh, A.S. Maan, A. Ohlan, Conducting polymer hydrogel based electrode materials for supercapacitor applications, J. Energy Storage 45 (2022) 19.
[23] R. Chakraborty, K. Vilya, M. Pradhan, A.K. Nayak, Recent advancement of biomass-derived porous carbon based materials for energy and environmental remediation applications, J. Mater. Chem. A 10 (2022) 6965–7005.
[24] J.H. Kang, J. Lee, J.W. Jung, J. Park, T. Jang, H.S. Kim, J.S. Nam, H. Lim, K. R. Yoon, W.H. Ryu, et al., Lithium-air batteries: Air-breathing challenges and perspective, ACS Nano 14 (2020) 14549–14578.
[25] A.F.M. EL-Mahdy, T.C. Yu, S.W. Kuo, Synthesis of multiple heteroatom-doped mesoporous carbon/silica composites for supercapacitors, Chem. Eng. J. 414 (2021) 15.
[26] B.F. Zhang, Y.L. Xu, J. Wang, X.N. Ma, W.Q. Hou, X. Xue, Electrochemical performance of LiFePO4/graphene composites at low temperature affected by preparation technology, Electrochim. Acta 368 (2021) 7.
[27] Y.C. Zhang, F.Q. Bai, Y.F. Xie, M.H. Zhu, L. Zhao, D.Q. An, D.M. Xue, E.B. Berda, C. Y. Wang, G.Y. Lu, et al., A conjugated polymer with Electron-withdrawing cyano group enables for flexible asymmetric electrochromic supercapacitors, Chem. Eng. J. 450 (2022) 11.
[28] Y. Wang, W. Zhang, H. Meng, J. Duan, Y. Zhang, Z. Xia, Y. Wang, Distinctive coordination configuration and interfacial water balance induced by Anti-Kirkendall effect attain exceptional catalytic activity and selectivity, Angew. Chem. Int. Ed. (2025) e13687.
[29] W. Yang, P. Wang, Z.Q. Tu, L.Q. Hou, L. Yan, B. Jiang, C.X. Zhang, G.Y. Huang, F. Yang, Y.F. Li, Heteroatoms-doped hierarchical porous carbon with multi-scale structure derived from petroleum asphalt for high-performance supercapacitors, Carbon 187 (2022) 338–348.
[30] T.L. Yang, J.Y. Chen, S.W. Kuo, C.T. Lo, A.F.M. EL-Mahdy, Hydroxyl-functionalized covalent organic frameworks as high-performance supercapacitors, Polymers 14 (16) (2022) 3428.
[31] Y.M. Nabil, S. Abdelnaser, A.A. Mohammed, S.W. Kuo, A.F.M EL-Mahdy, Engineering redox-active Benzo[1,2-b:4,5-b']dithiophene-Based conjugated polymers: tuning porosity and linker architecture for high-performance supercapacitors, J. Mater. Chem. A 13 (2025) 26337–26349.
[32] S.S. Sekhon, J.S. Park, Biomass-derived N-doped porous carbon nanosheets for energy technologies, Chem. Eng. J. 425 (2021) 19.
[33] S.G. Eswaran, M. Rashad, A.S.K. Kumar, A.F.M. EL-Mahdy, A comprehensive review of MXene-Based emerging materials for energy storage applications and future perspectives, Chem. Asian J. 20 (4) (2025) e202401181.
[34] X.F. Guo, G.J. Zhang, C.L. Wu, J. Liu, G.Q. Li, Y.Q. Zhao, Y. Wang, Y. Xu, A cost-effective synthesis of heteroatom-doped porous carbon by sulfur-containing waste liquid treatment: as a promising adsorbent for CO2 capture, J. Environ. Chem. Eng. 9 (2021) 11.
[35] J. Li, Y.J. Zou, C.L. Xiang, F. Xu, L.X. Sun, B. Li, J. Zhang, Osmanthus fragrans-derived N-doped porous carbon for supercapacitor applications, J. Energy Storage 42 (2021) 9.
[36] Y.F. Zheng, K.M. Chen, K.P. Jiang, F.R. Zhang, G.S. Zhu, H.R. Xu, Progress of synthetic strategies and properties of heteroatoms-doped (N, P, S, O) carbon materials for supercapacitors, J. Energy Storage 56 (2022) 12.

[37] X.C. Ma, C.Q. Su, B.G. Liu, Q.D. Wu, K. Zhou, Z. Zeng, L.Q. Li, Heteroatom-doped porous carbons exhibit superior CO2 capture and CO2/N2 selectivity: understanding the contribution of functional groups and pore structure, Sep. Purif. Technol. 259 (2021) 8.
[38] J.H. Zhan, A.F.M. EL-Mahdy, Redox-active Benzodithiophene-4,8-dione-Based conjugated microporous polymers for high-performance faradaic supercapacitor energy storage, Chem. Eng. J. 473 (2023) 11.
[39] M. Ahmed, A.F.M. EL-Mahdy, Multistep continuous synthesis of a highly fluorescent troger's base-derived benzoxazine: its thermal conversion into intrinsic microporosity polymers, Macromolecules 57 (2024) 5472–5485.
[40] S. Mukherjee, B. Lochab, Hydrogen bonding-guided strategies for thermal performance modulation in biobased oxazine ring-substituted benzoxazine thermosets, Macromolecules 57 (2024) 1795–1807.
[41] R. Yang, R.C. Yang, S.F. Yang, K. Zhang, Hydrogen bonding-rich bio-benzoxazine resin provides high-performance thermosets and ultrahigh-performance composites, ACS Sustain. Chem. Eng. 12 (2024) 1728–1739.
[42] A.F.M. EL-Mahdy, F.W. Lin, W.H. Su, T. Chen, S.W. Kuo, Photoresponsive azobenzene materials based on pyridine-functionalized benzoxazines as surface relief gratings, ACS Appl. Polym. Mater. 2 (2) (2019) 791–804.
[43] A.F. Saber, A.F.M. EL-Mahdy, S.W. Kuo, Development of heteroatom-rich fluorene-based benzoxazine-linked porous organic polymers as potential candidates for energy storage, J. Taiwan Inst. Chem. Eng. 168 (2025) 9.
[44] T. Periyasamy, S.P. Asrafali, J.W. Lee, High-performance supercapacitor electrodes from fully biomass-based polybenzoxazine aerogels with porous carbon structure, Gels 10 (2024) 15.
[45] R. Morales-Ospino, R.L.S. Canevesi, S. Schaefer, A. Celzard, V. Fierro, Is heteroatom doping of activated carbons always a good strategy for enhancing CO2 adsorption? Chem. Eng. J. 479 (2024) 14.
[46] R. Yang, Q. Chen, W.C. Sheng, K. Zhang, Oxazine ring-containing polycyclic monomers: a class of benzoxazine thermosetting resins with intrinsically low curing temperature, Macromolecules 57 (2024) 5608–5619.
[47] F.S. AlHumaidan, M.S. Rana, M. Vinoba, H.M. AlSheeha, A.A. Ali, R. Navvamani, Synthesis of graphene derivatives from asphaltenes and effect of carbonization temperature on their structural parameters, RSC Adv. 13 (12) (2023) 7766–7779.
[48] M. Ayiania, E. Weiss-Hortala, M. Smith, J.S. McEwen, M. Garcia-Perez, Microstructural analysis of nitrogen-doped char by raman spectroscopy: raman shift analysis from first principles, Carbon 167 (2020) 559–574.
[49] S. Zhi, Q. Dai, H. Wang, D. Wu, L. Zhao, C. Hu, L. Dai, Heteroatom-doped carbon materials for multifunctional noncatalytic applications, ACS Nano 19 (33) (2025) 29860–29897.
[50] E.B. Yılmaz, E.O. Eren, T. Horner, Z. Song, Y. Sheidaei, I. Siewert, E. Senokos, P. Giusto, Reductive carbon materials: tailoring chemistry and electronic properties to improve sodium-ion batteries, Angew. Chem. Int. Ed. 64 (13) (2025) e202422714.
[51] X. Xu, K. Sielicki, J. Min, J. Li, C. Hao, X. Wen, X. Chen, E. Mijowska, One-step converting biowaste wolfberry fruits into hierarchical porous carbon and its application for high-performance supercapacitors, Renew. Energy 185 (2022) 187–195.
[52] J.A. Nisha, J. Janaki, V. Sridharan, G. Padma, M. Premila, T.S. Radhakrishnan, X-ray diffraction and thermoanalytical investigations of amorphous carbons derived from C_{60}, Thermochim. Acta 286 (1) (1996) 17–24.
[53] Y. Wen, K. He, Y. Zhu, F. Han, Y. Xu, I. Matsuda, Y. Ishii, J. Cumings, C. Wang, Expanded graphite as superior anode for sodium-ion batteries, Nat. Commun. 5 (1) (2014) 4033.
[54] J. Wang, F. Qin, Z. Guo, W. Shen, Oxygen- and nitrogen-enriched honeycomb-like porous carbon from *Laminaria japonica* with excellent supercapacitor performance in aqueous solution, ACS Sustain. Chem. Eng. 7 (13) (2019) 11550–11563.
[55] X. Wang, M. Lou, X. Yuan, W. Dong, C. Dong, H. Bi, F. Huang, Nitrogen and oxygen dual-doped carbon nanohorn for electrochemical capacitors, Carbon 118 (2017) 511–516.
[56] E. Frackowiak, F. Béguin, Carbon materials for the electrochemical storage of energy in capacitors, Carbon 39 (6) (2001) 937–950.
[57] X. Zhao, Y. Zhou, Y. Xu, C. Huang, Y. Shen, Y. Zhang, Z. Fan, Q. Tang, A. Hu, X. Chen, Customizing oxygen-containing functional groups for reduced graphene oxide film supercapacitor with high volumetric performance, J. Energy Storage 52 (2022) 104642.
[58] W. Liu, M. Ulaganathan, I. Abdelwahab, X. Luo, Z. Chen, S.J.R. Tan, X. Wang, Y. Liu, D. Geng, Y. Bao, J. Chen, Two-dimensional polymer synthesized via solid-state polymerization for high-performance supercapacitors, ACS Nano 12 (1) (2018) 852–860.
[59] S.X. Liao, A.F.M. EL-Mahdy, Redox-active conjugated microporous polymers featuring a precise pore size for high-performance supercapacitor energy storage, ACS Appl. Energy Mater. 8 (5) (2025) 3074–3086.
[60] A.F. Saber, S.W. Kuo, A.F.M. EL-Mahdy, Microporous carbons derived from nitrogen-rich triazatruxene-based porous organic polymers for efficient cathodic supercapacitors, J. Mater. Chem. A 12 (25) (2024) 15373–15385.
[61] A.F.M. EL-Mahdy, T.C. Yu, S.W. Kuo, Synthesis of multiple heteroatom–doped mesoporous carbon/silica composites for supercapacitors, Chem. Eng. J. 414 (2021) 128796.
[62] S. Abdelnaser, S.W. Kuo, A.F.M. EL-Mahdy, Conjugated microporous polymers incorporating pyridine moieties for efficient faradaic supercapacitor energy storage, J. Power Sources 635 (2025) 236535.
[63] C. Sengottaiyan, R. Jayavel, R.G. Shrestha, T. Subramani, S. Maji, J.H. Kim, J. P. Hill, K. Ariga, L.K. Shrestha, Indium oxide/carbon nanotube/reduced graphene oxide ternary nanocomposite with enhanced electrochemical supercapacitance, Bull. Chem. Soc. Jpn. 92 (3) (2019) 521–528.
[64] A.F. Saber, S.U. Sharma, J.T. Lee, A.F.M. EL-Mahdy, S.W. Kuo, Carbazole-conjugated microporous polymers from suzuki–miyaura coupling for supercapacitors, Polymer 254 (2022) 125070.
[65] M. Ahmed, M.G. Kotp, T.H. Mansoure, R.H. Lee, S.W. Kuo, A.F.M. EL-Mahdy, Ultrastable carbazole-tethered conjugated microporous polymers for high-performance energy storage, Microporous Mesoporous Mater. 333 (2022) 111766.
[66] H. Zhang, G. Cao, W. Wang, K. Yuan, B. Xu, W. Zhang, J. Cheng, Y. Yang, Influence of microstructure on the capacitive performance of polyaniline/carbon nanotube array composite electrodes, Electrochim. Acta 54 (4) (2009) 1153–1159.
[67] T.A. Gaber, L.R. Ahmed, A.F.M. EL-Mahdy, Efficient faradaic supercapacitor energy storage using redox-active Pyrene- and Benzodithiophene-4,8-dione-Tethered conjugated microporous polymers, J. Mater. Chem. A 11 (36) (2023) 19408–19417.
[68] C. Young, J. Kim, Y.V. Kaneti, Y. Yamauchi, One-step synthetic strategy of hybrid materials from bimetallic metal–organic frameworks for supercapacitor applications, ACS Appl. Energy Mater. 1 (5) (2018) 2007–2015.
[69] V.V. Kondratiev, R. Holze, Intrinsically conducting polymers and their combinations with redox-active molecules for rechargeable battery electrodes: an update, Chem. Pap. 75 (10) (2021) 4981–5007.
[70] S. Huang, J. Shen, Y. Wu, X. Li, Y. Ma, Y. Xie, C. Yu, Y. Zhang, J. Zhang, $Bi_2O_2CO_3$ co-catalyst modification BiOBr driving efficient photoreduction CO_2, Colloids Surf. A Physicochem. Eng. Asp. 725 (2025) 37731.
[71] P. Raveendran, Y. Ikushima, S.L. Wallen, Polar attributes of supercritical carbon dioxide, Acc. Chem. Res. 38 (6) (2005) 478–485.
[72] J. Bai, J. Shao, Q. Yu, M. Demir, B.N. Altay, T.M. Ali, Y. Jiang, L. Wang, X. Hu, Sulfur-doped porous carbon adsorbent: a promising solution for effective and selective CO_2 capture, Chem. Eng. J. 479 (2024) 147667.
[73] X. Ma, C. Su, B. Liu, Q. Wu, K. Zhou, Z. Zeng, L. Li, Heteroatom-doped porous carbons exhibit superior CO_2 capture and CO_2/N_2 selectivity: understanding the contribution of functional groups and pore structure, Sep. Purif. Technol. 259 (2021) 118065.